



*Brno University of Technology*  
*Student Branch*

---

**Proceedings of IEEE Student Branch Conference**

# **Mikulov**

**2019**

**9. - 11. 9.**

---

**Název:** Proceedings of IEEE Student Branch Conference Mikulov 2019  
**Editor:** Miroslav Cupal  
**Vydavatel:** Vysoké učení technické v Brně  
Fakulta elektrotechniky a komunikačních technologií  
**Rok vydání:** 2019  
**Vydání:** první

**Organizační výbor konference:**

Ing. Erik Herceg  
Ing. Miroslav Cupal

Tato publikace neprošla jazykovou úpravou.  
Za obsah, původnost a literární citace odpovídají autoři jednotlivých příspěvků.

**ISBN 978-80-214-5781-2**

Conference was supported by

Gold sponsors



**Applus<sup>+</sup>**  
**IDIADA**

Bronze sponsors



Other partners



# Preface

Dear friends,

it is already for the 15th time when you can read the Proceedings of a conference organized by IEEE Student Branch, Brno University of Technology. In its reborn tradition, we are happy to welcome you at the conference for recent and future PhD students.

The aim of the conference was always to bring together young scientist to share their ideas and to have the possibility of familiarizing with the research at other departments and universities and this year will not be an exception.

Organizing a conference is never an easy task. Therefore, we would like to thank all the companies and organizations that supported us, namely Rohde & Schwarz, IDIADA, Era and URC Systems. Big thank you also belongs to IEEE Czechoslovakia Section and Department of Radio Electronics, Brno University of Technology.

To conclude, allow me to thank you, the participants of this year conference. By your participation, you support the very idea of what IEEE represents. We wish you a pleasant time in Mikulov.

On behalf of the organizers

Erik Herceg

# About URC Systems

URC Systems has been developing the comprehensive solutions to address the demanding needs of our customers since 1998. Our complete value chain provided to our customers contains research and development, manufacturing, after-sale service and user training in the areas:

- command and control of combat and electronic surveillance, reconnaissance and radio jamming,
- police command, control and service performance,
- data communication and integration.



## Research and development



We perform security and defence research projects. We develop special hardware, firmware, and software. We participate in strategic concepts for the Police of the Czech Republic, the Army of the Czech Republic and NATO. We cooperate with Czech and international universities and research institutions.

## Manufacturing and integration



We manufacture jammers for protection from activation of radio-controlled improvised explosive devices, ruggedized computers, radio elements and reconnaissance sets, including their integration into vehicles. We do system integrations at the level of software components, applications, and subsystems.

## Training and education



We develop simulators to facilitate training for our users. We offer training and education courses as part of implementation of new systems and innovations in our product portfolio.

## Servicing and maintenance



We provide servicing and maintenance as an integral part of the life cycle of our products. Our company is certified service center for THALES radio stations. We perform installation, configuration, and administration of workstations and servers for LINUX and MS Windows operating systems.

**URC Systems, spol. s r.o.**

Certification ISO 9001:2016, 14001:2016 | AQAP 2110

[www.urc-systems.com](http://www.urc-systems.com) | [sales@urc-systems.cz](mailto:sales@urc-systems.cz)

Head office: Zahovická 156b, 798 11 Prostějov, Czech Republic, tel: +420 582 337 255

# Table of content

<b>Nykrýnová Markéta</b>	
Method for improving the consensus sequence from NGS data based on reads classification	6
<b>Jurečková Kateřina</b>	
Pipeline for visualization of gene expression profiles of <i>Clostridium beijerinckii</i> NRRL B-598	10
<b>Cupal Miroslav</b>	
Smart seat for small airplanes	13
<b>Kokolia Martin</b>	
Textile Integrated Waveguide Sensors for Smart Vehicle Interior Upholstery	16
<b>Pokorný Josef</b>	
Improving of efficiency wireless	20
<b>Bartoň Vojtěch</b>	
Watershed Segmentation for Peak Picking of High-Resolution Mass Spectrometry Data	23
<b>Gotthans Jakub</b>	
Crest Factor Reduction and Digital Predistortion under Nonlinear Power Amplifier	26
<b>Bravenec Tomáš</b>	
Multiplatform System for Hand Gesture Recognition	30
<b>Kaděra Petr</b>	
Design of lens antennas for E-band communication	34
<b>Skryja Petr</b>	
System for analysis of FSO terminal vibrations	38
<b>Kerndl Michal</b>	
Hardware cryptographic module for FPGA with dynamic hash functions routing	39
<b>Herceg Erik</b>	
Wifi Access Point Detector	42
<b>Hrabina Martin</b>	
Optimization of Mel-Frequency Cepstral Coefficients for Gunshot Detection	46
<b>Krutílek David</b>	
Advanced methods of lightning protection of composite aircraft	49

# Method for improving the consensus sequence from NGS data based on reads classification

Markéta Nykrýnová, Helena Škutková  
 Department of Biomedical Engineering  
 Brno University of Technology  
 Brno, Czech Republic  
 Email: nykrynova@vutbr.cz, skutkova@vutbr.cz

**Abstract**—Nowadays, next-generation sequencing is on the rise as a cost of sequencing is constantly dropping. However, the processing of the sequence data remains problematic as the algorithms for reference-based assembly are both computationally and time-demanding. Moreover, resulting assembly is still imperfect. In this paper, we present a new method for improving the quality of the consensus sequence from the assembled data. We examine the regions in the consensus sequence, which show a high number of ambiguous nucleotides. Using a classification of reads covering these regions, we try to reduce the number of ambiguous nucleotides in the consensus. This improved consensus sequence then can be used for bacteria typing and precise discrimination of bacteria strains.

**Keywords**—sequencing; ambiguous nucleotides; genome assembly; consensus calling; cluster analysis

## I. INTRODUCTION

Typing of bacteria is a process, which leads to the identification of relationships between bacterial strains of the same species [1]. In medical facilities, typing is used practically every day, because it allows us to distinguish between resistant and non-resistant bacteria. Also, it helps us to understand the spreading patterns of infection and find its source [2].

Because the bacterial population in one hospital or even within one hospital department is closely related, the whole genomes differ only in a few nucleotides. So that NGS (next-generation sequencing) is used for typing of closely related bacterial strains as it can find single nucleotides mutation among bacterial strains [3]. Additionally, the cost of NGS is decreasing, so it becomes more readily available for everyday routine typing [4]. On the other hand, despite the growing amounts of sequenced data, the postprocessing of data is still imperfect [5].

During genome sequencing, a large number of reads from 50 bp to 100 kb are produced [4]. These reads are then assembled based on overlap (*de novo* assembly) or mapped to the reference sequence, and as a result, a consensus sequence of the genome is created.

When reads are mapped to the reference sequence, some problems can occur. If chosen reference differs from sequenced genomes, the assembly may not work correctly, and some reads, which can contain even genes can be labelled as unmapped. Another problem can occur with duplicate regions in genomes, where corresponding reads can be ignored or

distributed evenly on repetitive sequences. Reads also can be placed randomly on one location in the genome, or they can all be placed in the first position of occurrence [6], [7].

During consensus calling from assembled reads, a problem with ambiguous positions in the genome may occur. As already is mentioned above, if repetitive sequences are mapped to one location to reference genome and one of the repetitive elements contains some mutations, after mapping to one location, two nucleotide bases can occur in one position across reads. As a result, ambiguous nucleotide appears in the consensus according to IUPAC coding, as is shown in the fig. 1. The same problem may arise if a sequencing data contains not only chromosome DNA but also plasmid DNA. Reads from both DNA can be very similar, thus during assembly reads can be mapped to one location which leads to ambiguous nucleotides in the consensus sequence [8]. The ambiguous nucleotides in the consensus sequence increase variability between bacterial strains. Therefore bacterial typing can give inaccurate results.

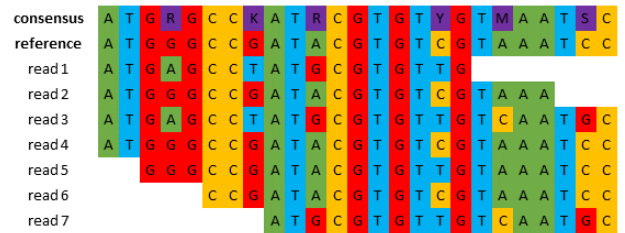


Fig. 1. Example of reference-based assembly and obtained consensus sequence.

The goal of our project is to find regions in consensus sequences with a high number of ambiguous nucleotides and classify reads which are mapped to this region to two clusters and determinate which cluster can be used for final consensus calling and which one is from another part of the bacterial genome.

In our project, we worked with a genome of *Enterococcus faecium*, which is Gram-positive bacteria, and it can be found in the gastrointestinal tract of humans [9]. In the last years, it causes hospital-acquired infections such as wound infections, neonatal sepsis, bacteremia, and many other [10].

## II. MATERIALS AND METHODS

In this project, we worked with the genomes of *Enterococcus faecium*. The bacterium was collected from the Department of Internal Medicine, Hematology and Oncology of University Hospital Brno.

Our method consists of several steps which are described in the following paragraphs. First, the genome must be sequenced, and obtained data must be assembled. Then, the consensus sequence is generated, and ambiguous regions are identified. Reads which cover ambiguous regions are extracted and clustered. From obtained clusters, new consensus sequences are generated and using BLAST algorithm, the final consensus for the ambiguous region is selected. The block diagram of the proposed method is shown in the fig. 2.

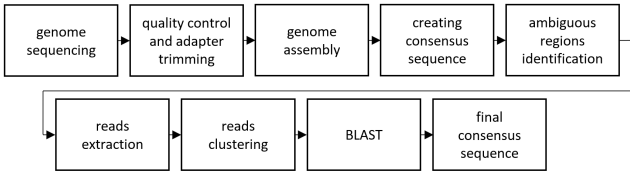


Fig. 2. Block diagram of the proposed method.

### A. Genome assembly

The obtained samples were sequencing on Illumina MiSeq. As a result, we obtained paired-end reads with an average length of 250 bp. Before genome assembly, the quality of sequence data was examined by FastQC [11] and MultiQC [12].

After the quality control, the adapter trimming was done using Trimmomatic [13]. Then the genomes were assembled to reference *Enterococcus faecium* *Aus0004* which was obtained from NCBI database (NC\_017022.1). The Burrows-Wheeler Aligner MEM [14], which is recommended for Illumina data, was used for genome assembly.

In the next step, we used Samtools [15] to remove potential PCR duplicates and optical duplicates. Also, unmapped reads and not properly paired reads were removed from the assembly. Reads which did not pass quality controls and mapping quality is smaller than 20 and minimum base quality 20 were removed. After that, the consensus sequences were generated.

### B. Ambiguous sequence detection

In the consensus sequences of *Enterococcus faecium* the regions with a high number of ambiguous nucleotides are detected. The floating window of length 250 bp is moving alongside the sequence with a shift of 1 nucleotide and the number of ambiguous nucleotides within the window is calculated. If the number exceeds 25 nucleotides, the beginning of the ambiguous region is marked. The window moves, and when the number of ambiguous nucleotides decreases under 25, the end of the region is signed. As a result, a list of coordinates in sequences with ambiguous nucleotides is obtained.

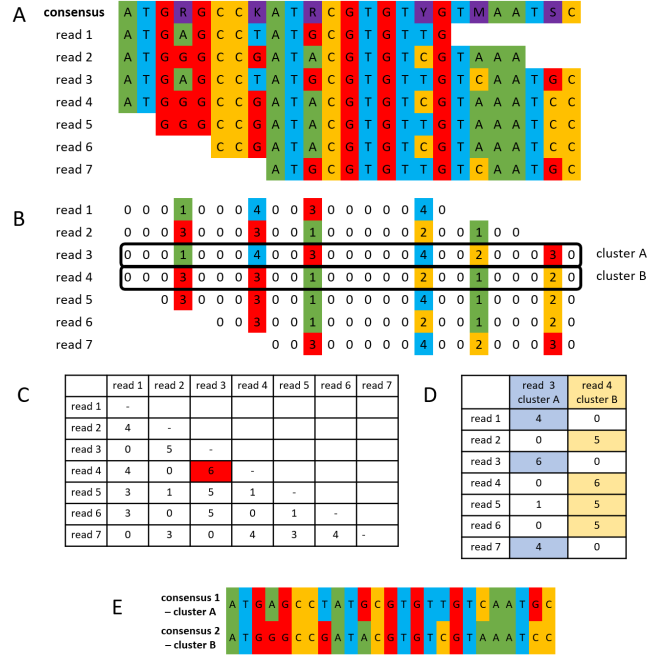


Fig. 3. A. Example of genome assembly. B. Reads with assigned numbers in ambiguous positions. C. Matrix of mismatches between reads. D. Matrix of matches between reads and given clusters. E. Consensus sequences from obtained clusters.

### C. Extracting reads

In the next step, the reads extraction is conducted. Reads are extracted from SAM file, which contains proper paired, and high quality reads. The reads which are mapped 250 bp before the start of the region with ambiguous nucleotides and ended 250 bp before the end of this region are extracted from the file. The number of 250 bp was chosen because it is the average length of the reads.

Because reads are aligned to the reference sequence based on local alignment, some parts of the reads do not have to be a part of the final alignment. To find out which parts of reads are used for final alignment, the CIGAR (Compact Idiosyncratic Gapped Alignment Report) string is used. It describes which part of reads were mapped to reference, which were clipped off and it also contains information about deletion or insertion of nucleotides. Using CIGAR string information, we extract only the part of reads which were used for mapping and for the final consensus calling.

### D. Clustering

In the next part of the project, reads are classified into two clusters. An example of a clustering process is shown in fig. 3.

As the first step, to each read for every ambiguous position numbers are assigned as follows, A  $\rightarrow$  1, C  $\rightarrow$  2, G  $\rightarrow$  3, T  $\rightarrow$  4 and N  $\rightarrow$  5. To all other positions, 0 is noted, and a matrix is created (fig. 3B).

In the second step, each read (row of the matrix) is compared to all another reads. Only the positions where both reads contain non-zeros numbers are compared. As a result,

the matrix of mismatches between reads is obtained (fig. 3C). In this matrix, the maximum, which corresponds to the most different reads, is located. Reads corresponding to the maximum are used as templates for classification.

Remaining reads are then assigned to these two groups based on the number of matches (fig. 3D). If a read can be classified to both clusters, it is eliminated from the analysis.

As a result, two clusters of reads are created. For each cluster, a consensus sequence is created (fig. 3E). The consensus sequences are then analyzed using the BLAST algorithm [16].

### III. RESULTS

We worked with 4 genomes of *Enterococcus faecium* of length 2 955 294 bp. Basic information about this genomes are shown in the table I.

TABLE I. GENOMES OF *Enterococcus faecium*.

name of genome	number of reads	number of mapped reads	mean coverage
ENFI_47	1 834 764	1 217 434	85.21
ENFI_176	1 448 111	957 722	71.52
ENFI_58	1 643 987	1 075 829	81.20
ENFI_163	940 164	628 285	41.03

In these genomes, regions with a higher number of ambiguous nucleotides were located and examined. In total, twelve regions were identified, whereas in one genome four regions were located, in two genomes, three regions were identified, and two regions were discovered in one genome.

Using BLAST algorithm was found out if created consensus sequences from reads classification contain chromosome or plasmid DNA. In BLAST output, all sequences which producing significant alignments and their query cover were 100 % were examined. As a result, the ratio of sequences containing chromosome or plasmid DNA to all sequences was established.

In seven cases, the first obtained consensus sequence contained chromosome DNA and the second consensus sequence contained plasmid DNA. Thus, the ambiguous regions in the original consensus sequences of *Enterococcus faecium* can be substitute with consensus of chromosome DNA which were created during reads classification.

In three cases, only chromosome DNA was present. It may imply that corresponding regions are repetitive sequences, but genome assembler assigns all reads to one location.

In two cases, one consensus sequence was identified as a part of chromosome DNA, and in the second one, both plasmid and chromosome DNA were present. In these cases, classification to more than two clusters should be considered.

Obtained results are shown in tables II, III, IV, V.

### IV. CONCLUSION

In this paper, we present a new approach for improving the consensus sequences of the assembled genomes of *Enterococcus faecium*. Regions in consensus sequences with a high number of ambiguous nucleotides were identified, and corresponding reads were extracted. After that, reads were

TABLE II. AMBIGUOUS REGIONS IN THE GENOME ENFI\_47 AND RESULTS FROM BLAST ANALYSIS.

id	start of region	end of region	length of region [bp]	number of ambiguous nucleotides	
1	74430	74799	370	33	
2	74832	75480	649	62	
3	2807042	2807516	475	43	
		consensus 1		consensus 2	
id	chromosome DNA	plasmid DNA	chromosome DNA	plasmid DNA	
1	0/31	31/31	146/147	1/147	
2	0/31	31/31	146/147	1/147	
3	75/249	174/249	13/13	0/13	

TABLE III. AMBIGUOUS REGIONS IN THE GENOME ENFI\_176 AND RESULTS FROM BLAST ANALYSIS.

id	start of region	end of region	length of region [bp]	number of ambiguous nucleotides	
1	74463	74799	337	27	
2	75025	75555	531	55	
3	2422679	2423042	364	31	
4	2807042	2807516	475	43	
		consensus 1		consensus 2	
id	chromosome DNA	plasmid DNA	chromosome DNA	plasmid DNA	
1	0/31	31/31	146/147	1/147	
2	0/31	31/31	144/145	1/145	
3	62/62	0/62	43/43	0/43	
4	13/13	0/13	79/79	0/79	

TABLE IV. AMBIGUOUS REGIONS IN THE GENOME ENFI\_58 AND RESULTS FROM BLAST ANALYSIS.

id	start of region	end of region	length of region [bp]	number of ambiguous nucleotides	
1	74427	75555	1129	119	
2	2807042	2807516	475	43	
		consensus 1		consensus 2	
id	chromosome DNA	plasmid DNA	chromosome DNA	plasmid DNA	
1	0/31	31/31	146/147	1/147	
2	75/249	174/249	79/79	0/79	

TABLE V. AMBIGUOUS REGIONS IN THE GENOME ENFI\_163 AND RESULTS FROM BLAST ANALYSIS.

id	start of region	end of region	length of region [bp]	number of ambiguous nucleotides	
1	74427	75555	1129	116	
2	2422679	2423042	364	31	
3	2807040	2807516	477	44	
		consensus 1		consensus 2	
id	chromosome DNA	plasmid DNA	chromosome DNA	plasmid DNA	
1	0/31	31/31	146/147	1/147	
2	62/62	0/62	43/43	0/43	
3	75/251	176/251	79/79	0/79	

classified into two clusters. From clusters, consensus sequences were generated and then examined via BLAST.

We were capable of distinguishing sequences from chromosomes and plasmids. Thus, sequences of chromosome DNA can be added to original consensus sequences to reduce the number of ambiguous nucleotides. As a result, a more precise comparison of genomes can be made. Also, in the bacterial genomes, we discovered sequences which can be repetitive elements. Thus, further analysis of these sequences can be done.

The drawback of our method is high sensitivity to the quality of sequenced data. Also, a choice of genome assembler and reference genome must be done carefully as a number of mapped reads can vary up to 10 % and different consensus

sequence can be obtained.

Our methodology was designed for *Enterococcus faecium*, but it can be used for any bacteria, and in the future, our method will be fully automatized.

#### ACKNOWLEDGMENT

This work was supported by grant project of the Czech Science Foundation [GACR 17-01821S].

#### REFERENCES

- [1] A. J. Sabat, A. Budimir, D. Nashev, R. Sá-Leão, J. M. V. Diji, F. Laurent, H. Grundmann, A. W. Friedrich, and On Behalf Of The Escmid Study Group, "Overview of molecular typing methods for outbreak detection and epidemiological surveillance," *Eurosurveillance*, vol. 18, no. 4, 2013.
- [2] R. Ranjbar, A. Karami, S. Farshad, G. M. Giammanco, C. Mammina, "Typing methods used in the molecular epidemiology of microbial pathogens: a how-to guide," *New Microbiologica*, vol. 37, pp. 1-15, 2014.
- [3] W. Ruppitsch, "Molecular typing of bacteria for epidemiological surveillance and outbreak investigation / Molekulare Typisierung von Bakterien für die epidemiologische Überwachung und Ausbruchsabklärung," *Die Bodenkultur: Journal of Land Management, Food and Environment*, vol. 67, no. 4, pp. 199–224, 2016.
- [4] J. Besser, H. Carleton, P. Gerner-Smidt, R. Lindsey, and E. Trees, "Next-generation sequencing technologies and their application to the study and control of bacterial infections," *Clinical Microbiology and Infection*, vol. 24, no. 4, pp. 335–341, 2018.
- [5] S. El-Metwally, T. Hamza, M. Zakaria, and M. Helmy, "Next-Generation Sequence Assembly: Four Stages of Data Processing and Computational Challenges," *PLoS Computational Biology*, vol. 9, no. 12, 2013.
- [6] I. Abnizova, R. T. Boekhorst, and Y. L. Orlov, "Computational Errors and Biases in Short Read Next Generation Sequencing," *Journal of Proteomics & Bioinformatics*, vol. 10, no. 1, 2017.
- [7] H. Li and R. Durbin, "Fast and accurate short read alignment with Burrows-Wheeler transform," *Bioinformatics*, vol. 25, no. 14, pp. 1754–1760, 2009.
- [8] S. Arredondo-Alonso, R. J. Willems, W. V. Schaik, and A. C. Schürch, "On the (im)possibility of reconstructing plasmids from whole-genome short-read sequencing data," *Microbial Genomics*, vol. 3, no. 10, 2017.
- [9] G. Castillo-Rojas, M. Mazari-Hirfart, S. P. D. León, R. I. Amieva-Fernández, R. A. Agis-Juárez, J. Huebner, and Y. López-Vidal, "Comparison of *Enterococcus faecium* and *Enterococcus faecalis* Strains Isolated from Water and Clinical Samples: Antimicrobial Susceptibility and Genetic Relationships," *PLoS ONE*, vol. 8, no. 4, 2013.
- [10] H. S. Kafil, M. Asgharzadeh, "Vancomycin-Resistant *Enterococcus faecium* and *Enterococcus faecalis* Isolated from Education Hospital of Iran," *Maedica*, vol. 9, no. 4, 2014.
- [11] S. Andrews, "FASTQC. A quality control tool for high throughput sequence data." 2010.
- [12] P. Ewels, M. Magnusson, S. Lundin, and M. Käller, "MultiQC: summarize analysis results for multiple tools and samples in a single report," *Bioinformatics*, vol. 32, no. 19, pp. 3047–3048, 2016.
- [13] A. M. Bolger, M. Lohse, and B. Usadel, "Trimmomatic: a flexible trimmer for Illumina sequence data," *Bioinformatics*, vol. 30, no. 15, pp. 2114–2120, 2014.
- [14] H. Li, "Aligning sequence reads, clone sequences and assembly contigs with BWA-MEM," *Antimicrobial Resistance & Infection Control*, 2013.
- [15] H. Li, B. Handsaker, A. Wysoker, T. Fennell, J. Ruan, N. Homer, G. Marth, G. Abecasis, and R. Durbin, "The Sequence Alignment/Map format and SAMtools," *Bioinformatics*, vol. 25, no. 16, pp. 2078–2079, 2009.
- [16] S. Altschul, "Basic Local Alignment Search Tool," *Journal of Molecular Biology*, vol. 215, no. 3, pp. 403–410, 1990.

# Pipeline for visualization of gene expression profiles of *Clostridium beijerinckii* NRRL B-598

Katerina Jureckova, Karel Sedlar, Ivo Provaznik

Department of Biomedical Engineering  
Brno University of Technology  
Brno, Czechia  
jureckova@feec.vutbr.cz

**Abstract**—Gene expression profiling is a key to understanding of the patterns of gene activity at the transcription level for example under different conditions. In specific cell it capture current state of genes' activity and give us a picture of cellular function together with connections to genomic features. In this study, we present a pipeline for processing of transcriptomic RNA-Seq data of *Clostridium beijerinckii* NRRL B-598 and visualization of gene expression profiles by heatmaps.

**Keywords**—RNA-Seq; gene expression profile; heatmap

## I. INTRODUCTION

Gene expression profiling is a key to understanding of the patterns of gene activity at the transcription level for example under different conditions. In specific cell it capture current state of genes' activity and give us a picture of cellular function together with connections to genomic features. Popular technique in transcriptomic is nowadays RNA-Seq that allow to measure activity of all genes in the sample at the same time. This technology uses next-generation sequencing (NGS) to examine the quantity and sequences of RNAs[1].

Gene expression profile can be visualized by heatmaps. Heatmap is graphical representation of values by colors. In transcriptomics, it is a simple but powerful tool for visualization of expression patterns across samples and genes and helps us to predict putative gene functions or involvement in biological process. Heatmap is usually created for groups of genes with putative relationship, which we can be shown in gene expression profiles by change of colors. Selection of genes plays key role in final graphical output. Heatmaps are very useful for small datasets, but with increasing size we lose information about similarities and differences present in dataset.

In this study we used RNA-Seq data of *Clostridium beijerinckii* NRRL B-598. This bacterial strain is gram positive, rod-shaped, spore forming and oxygen tolerant. We study *C. beijerinckii* NRRL B-598 for its ability to produce biofuels from biomass during ABE (acetone-butanol-ethanol) fermentation[2], [3].

## II. MATERIALS AND METHODS

### A. RNA-Seq data

In this paper we worked with cultivation samples of *Clostridium beijerinckii* NRRL B-598. Six samples were collected in irregular time intervals during cultivation with addition of butanol. Selected time points (6h, 6.5h, 7h, 8h, 10h, 12h) cover response to butanol shock performed after first sample collection. All samples had two replicates and library preparation and sequencing was conducted by the CEITEC Genomics core facility (Brno, Czechia) on Illumina NextSeq 500, single-end, 75 bp.

### B. Reads preprocessing and mapping

Raw RNA-Seq data in FASTQ format were preprocessed by Trimmomatic[4] and adaptors were trimmed. Further we removed transcripts and reads representing 16S and 23S rRNA by SortMeRNA[5] with help of SILVA database[6], that contains known bacterial 16S and 23S rRNA sequences.

Clean reads were than mapped by STAR software[7] to reference genome of *C. beijerinckii* NRRL B-598. Used genome assembly with annotation is available in GeneBank database under CP0011966.3 accession number (<https://www.ncbi.nlm.nih.gov/nucleotide/CP0011966.3>).

Output files were sorted and converted from Sequence Alignment Map (SAM) format to compressed Binary Alignment Map (BAM) format by SAMtools[8].

### C. Reads counting

To establish number of mapped reads to each annotated gene locus tag were performed reads counting based on received BAM files and gene transfer format (GTF) file of reference genome. GTF file contains genomic features, their coordinates, score, reading frame etc. and BAM files has information of overlap between reads and genomic features. Read counting was then performed by featureCounts function from Rsubread package[9] from R/Bioconductor. During counting we dealt with reads that were mapped to several locus tags. These reads were counted towards all related genomic features, but only as fractional counts and so the number of reads in the sample remains the same.

#### D. Count tables normalization

Obtained count tables represent quantity of transcripts present in the samples, but each sample has different library size, each gene has different length etc. In the next step, count tables were normalized by built-in function of DESeq2 package[10] from R/Bioconductor. After normalization, we can compare expression across all genomic features and samples present in dataset. Normalized counts from all replicates for particular time point of cultivation were in the end averaged before final visualization by heatmap.

#### E. Heatmap creation

In the last part we created heatmap from selected locus tags of *C. beijerinckii* NRRL B-598. Creation of heatmap was performed by gplots and RColorBrewer packages in R. Firstly Z-scores are estimated separately for each genomic feature and its time points from averaged normalized counts. From all Z-scores present in the selection, color key is evaluated and each interval of values received its color. And finally heatmap is created as an image.

For easier work with heatmap, we decided to recreated it in excel spreadsheet with conditional formatted cells. Creation of excel file was handled by openxlsx and magick packages in R. Pipeline process all text files in work directory and add new spreadsheet for each processed file. Input file has to be tab-delimited text files and contain log tags of genomic features and their annotation. Both information is added to heatmap for easier biological interpretation of gene expression profiles.

### III. RESULTS AND DISCUSSION

The main reason for creation of this pipeline was simplification and automation of process of creation of heatmaps for further biological interpretation of gene expression data. Problem of heatmaps is in their variability. Although Z-scores for each locus tag remains the same, the color representing their values change with selection of other genes present in heatmap. The color key always changes. This need to create new heatmap for each new selection of genes, led to this pipeline.

First part of pipeline deals with processing of unmapped reads and outputs averaged normalized count reads. The second part take care of automated generation of heatmaps from averaged normalized counts through Z-score calculation and color key estimation. The heatmap generator take as input text files with list of desired genomic features and create heatmap as image and as excel file with list of locus tags, their annotation and heatmap created by conditional formatting of excel cells (see Fig. 1.). We decided to use excel spreadsheet because, we often change order of locus tags and we add more information about genes right next to heatmap for example differential expression analysis. Results from this analysis helps us to evaluate which color change in heatmap was statistically significant and when the level of gene expression remains on the same level.

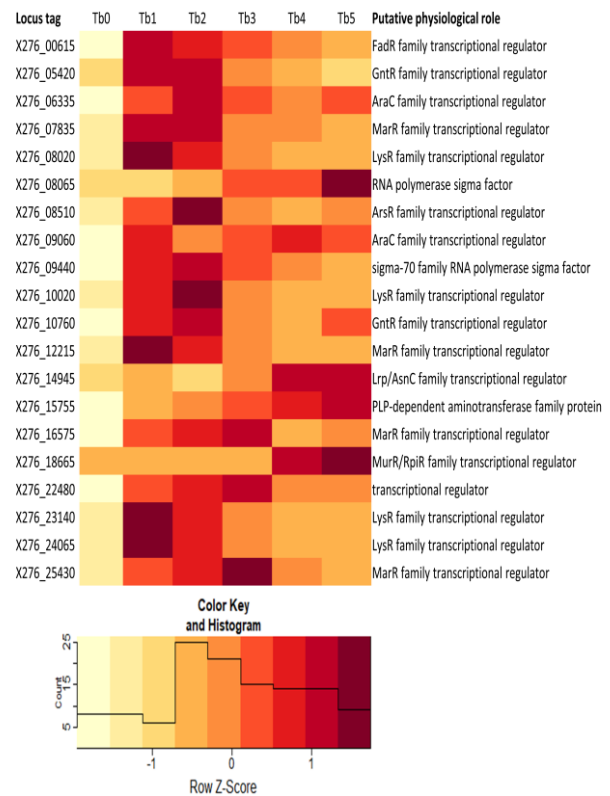


Fig. 1. Heatmap of genes involved in DNA-binding transcription factor activity molecular function.

In the future we plan to create a stand-alone application of this pipeline and enable access to heatmap creation to users without prior knowledge of programming in R. This application will enable user to choose, which experiment and replicates will be used for heatmap creation. User will be able to choose input files and input files will not have to contain gene annotation of each locus tag. Annotation will be added automatically. Application could be also further extended with addition of differential expression analysis to excel spreadsheet or other information relevant for biological interpretation of RNA-Seq data. In the best scenario this application will be available online and without a need to have R and its necessary packages installed.

### IV. CONCLUSION

Pipeline for visualization of gene expression profiles of RNA-Seq transcriptome was introduced. First part of pipeline process RNA-Seq transcriptomic data of *Clostridium beijerinckii* NRRL B-598 and provide averaged normalized counts representing gene expression profile for heatmap creation. Second part of pipeline deals with graphical output (heatmap) and automatically export heatmap as images and corresponding excel file. Pipeline is now realized in R and requires other R packages. In the future pipeline will be reworked into a stand-alone application for users without prior knowledge of programming.

#### ACKNOWLEDGMENT

This work has been supported by grant project GACR 17-00551S.

#### REFERENCES

- [1] Z. Wang, M. Gerstein, and M. Snyder, "RNA-Seq: a revolutionary tool for transcriptomics," *Nat. Rev. Genet.*, vol. 10, no. 1, pp. 57–63, Jan. 2009.
- [2] P. Patakova et al., "Acidogenesis, solventogenesis, metabolic stress response and life cycle changes in *Clostridium beijerinckii* NRRL B-598 at the transcriptomic level," *Sci. Rep.*, vol. 9, no. 1, p. 1371, 2019.
- [3] P. Patakova et al., "Comparative analysis of high butanol tolerance and production in clostridia," *Biotechnol. Adv.*, vol. 36, no. 3, pp. 721–738, May 2018.
- [4] A. M. Bolger, M. Lohse, and B. Usadel, "Trimmomatic: a flexible trimmer for Illumina sequence data," *Bioinformatics*, vol. 30, no. 15, pp. 2114–2120, Aug. 2014.
- [5] E. Kopylova, L. Noe, and H. Touzet, "SortMeRNA: fast and accurate filtering of ribosomal RNAs in metatranscriptomic data," *Bioinformatics*, vol. 28, no. 24, pp. 3211–3217, Dec. 2012.
- [6] C. Quast et al., "The SILVA ribosomal RNA gene database project: improved data processing and web-based tools," *Nucleic Acids Res.*, vol. 41, no. D1, pp. D590–D596, 2012.
- [7] A. Dobin et al., "STAR: ultrafast universal RNA-seq aligner," *Bioinformatics*, vol. 29, no. 1, pp. 15–21, Jan. 2013.
- [8] H. Li et al., "The Sequence Alignment/Map format and SAMtools," *Bioinformatics*, vol. 25, no. 16, pp. 2078–2079, Aug. 2009.
- [9] Y. Liao, G. K. Smyth, and W. Shi, "featureCounts: an efficient general purpose program for assigning sequence reads to genomic features," *Bioinformatics*, vol. 30, no. 7, pp. 923–930, Apr. 2014.
- [10] M. I. Love, W. Huber, and S. Anders, "Moderated estimation of fold change and dispersion for RNA-seq data with DESeq2," *Genome Biol.*, vol. 15, no. 12, p. 550, 2014.

# Smart seat for small airplanes

Miroslav Cupal

Brno University of Technology  
Department of Radioelectronics  
Brno, Czech Republic  
cupalm@phd.feec.vutbr.cz

**Abstract**—The paper presents an electronic system integrated into car or airplane seat independent on other systems and services. The seat can monitor some basic values like temperature, humidity or pressure on the seat or inside the cabin. The seat can be equipped by PID regulated heating system which can increase passengers comfort because small airplanes operates in far destinations and they are used as last-mile traffic. The telemetry is sent to central monitor unit via wireless network and data can be stored, analyzed or viewed by crew or passenger in special application. The seat is connected only to supply system (if heating is used) or can be supply by integrated battery.

**Keywords**—airplane; seat; sensors; textile integration

## I. INTRODUCTION

Textile integrated sensors became popular with the popularization of wearable applications for health and sport activity monitoring. These sensors can capture patients biological signals like ECG, breathing, temperature and humidity. Seats in automotive are equipped by sensors of passenger occupation, seat belt sensor or heating system. These sensors increase the comfort of passengers and their safety and cooperate with other systems in a car [1].

In the opposite side, the aviation industry is more conservative and safety requirements are on a higher level. Systems in airplanes are divided into four categories define the impact on safety. For this reason, the integration of new systems to the airplane is more complicated and some system changes cannot be implemented without certification of the whole airplane. The trend in flight transportation is the transport of maximum passengers in one airplane and cost minimization (low-cost airlines), but there are classic airlines where passengers comfort is in the first place.

The smart seat can improve passengers comfort or their safety because it can react to their needs. The integrated temperature sensor can measure the temperature and the humidity of each passenger and cooperate with air-conditioning if most the passengers feel discomfort. The pressure matrix sensor can inform the crew about passenger comfort during a long flight.

Because the developing of sensors is a pretty challenge, the commercially available sensors are used for construction smart

seat. The conductive threads, piezoresistive foils and on-chip solutions are used.

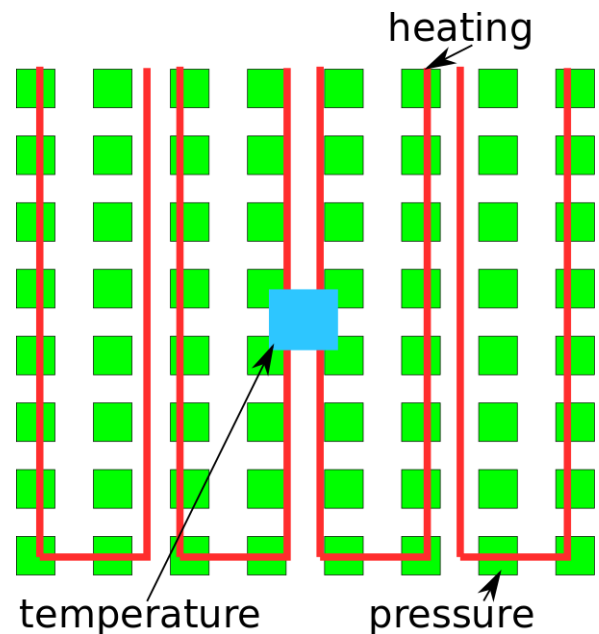


Fig. 1: Sensor integration schematic.

## II. SYSTEM DESIGN

The designed system is independent on other airplane systems and can be fed by battery (low power sensor system) or by airplane supply (complete system with heating). The MCU (microcontroller unit) used for driving and communication with sensors is ATmega 328. ATmega 328 is 8-bit/16 MHz MCU equipped by six 8-bit A/D converters and 16 digital IO pins and 6 PWM (pulse width modulation) pins [2]. Sensors integrated into the seat can capture temperature and humidity, seat occupation, moisture detection and can be expanded by the heating system. The MCU is connected to wireless module OWS-451 via UART. The OWS-451 is UART/Wi-Fi wireless module what can use ISM band 5.8 GHz and it can connect to laptop, smartphone or tablets via secure Wi-Fi. The OWS-451 is connected to textile integrated antenna. The antenna has monopole-like radiation patterns and allows to communicate in case if passenger on the

seat or not. The tablet can be used for presenting sensors data [3], [4].

### III. TEXTILE INTEGRATED SENSORS

#### A. Moisture sensor

The moisture sensor is created by conductive thread sewed to meanderings structure and the resistivity between two parallel thread is measured. A distance between two threads is 2 cm and the sensor can detect very low humidity only about 2 ml of water. Because the sensor is connected to A/D converter, the amount of moisture can be measured. The sensor is on all surface of the seat and can be divided into more sectors or be on the floor of the airplane. The sensor schematic is in Figure 1 and the photography of the sensor is in Figure 4.



Fig. 2: Pressure matrix sensor based on piezoresistive foil; matrix 8x8.

#### B. Temperature and humidity sensor

The integrated temperature and humidity sensor is used inside the seat. The sensor used for sensing is SHT21. This sensor allows measuring humidity from 0 to 100% and the temperature from -40 to 125 °C. The supply voltage of the chip is 3.3 V and the average power dissipation is 3.2  $\mu$ W. The SHT21 is connected to MCU by I2C and the temperature and humidity are measured with period 10 second. The physical connection to the MCU can be realized by conductive thread or by lacquered wire. If the connection is realized by the conductive thread, it is necessary to isolate the thread by lacquer or color because it is possible that the seat will be wet and uninsulated thread can be damaged by water.

#### C. Passenger occupation sensor

The pressure sensor is based on piezoresistive foil insert between two electrodes. The seat is equipped by matrix 8x8 created from the pressure sensor. The piezoresistive foil is inserted between perpendicular strips created by conductive fabric. The matrix is shown in Figure 2. One set of conductive fabric strips is covered by piezoresistive foil and the second set of strips is perpendicular. The width of the strips is between 1 and 0.5 cm. The foil can be used as one piece, but the strip solution increases passenger comfort (seat can breathe and transport humidity far from passenger). The fabric strips are connected to a multiplexer and A/D converter. The data

from the sensor are post-processed and the system decides if the seat is occupied by a passenger, some load (bag) or empty.

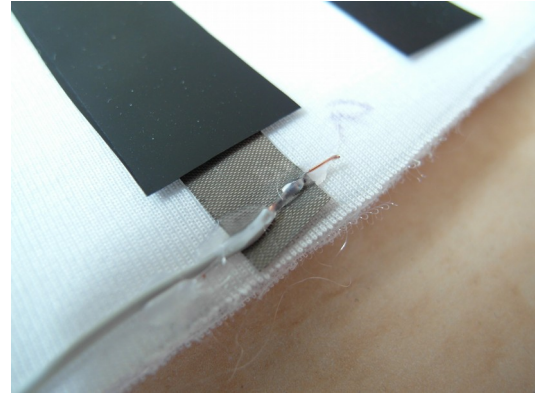


Fig. 3: Detail view to the soldered connection between the copper wire and conductive textile.

#### D. PID driven heating layer

Because the feeling temperature is different for each person, passenger can set the temperature of the seat and the power of the heating is automatically regulated by the PID regulator. This regulation allows increasing passengers comfort because common integrated heating systems allows set only some levels of power heating. The heating system is set to the maximum power of 30 W. Because the airplanes typical voltage is 12 V the maximal current consumption is 1.6 A. Because the voltage can vary between 11 and 18 V, the voltage is regulated by DC converter.

The PID regulator changes the PWM pulse width which can regulate the power of the heating layer. The temperature of the heating system is monitored and limited to safety value. The maximal temperature of the heating layer is 40°C. Passenger can set temperature by capacitive touch buttons installed close to the seat or on the seat.

#### E. Capacitive buttons

Because the temperature of the heating system can be driven by passenger it is necessary to drive it as easy as possible. The system can be driven by capacitive touch buttons integrated into the textile of the seat or upholstery of the airplane. The touch buttons allow ON/OFF heating and integrated light or set the temperature. The buttons are connected by lacquered wires to the MCU and they can be created by conductive textile, sheet, thread or conductive printed motive. The print technology allows creating different shapes of these buttons. For example like a plus, minus, bulb or some logo.

The ATmega 328 measures time constant created by a resistor and capacitive touch button. This system needs one send pin and more receive pins. The time constant of each RC changes if the surface of the button is touched. Because the sensor senses the capacitance of the human body, it can be covered by a thin layer of dielectric material as some fabric.

#### IV. TECHNOLOGICAL ASPECTS

Maximum of sensors is based on textile materials, the only thermometer is the on-chip solution. Conductive thread ELITEX® Art, SC 110/f34\_PA/Ag is used like heating system and humidity sensor and as “wires”. This thread is silver-based nylon thread with resistivity 15  $\Omega$ /m. Because this thread is not isolated, there are solutions for creating conductive isolated “wires”. It is possible to use lacquered wire commonly used for transformers. The second solution is using paint for textile. In this case, the lacquered wire is used for contact between sensors and MCU. The conductive wire can be stuck or soldered. There are conductive glues which can stick the wires with textile materials. The lacquer from the surface of the wire can be removed by heating. The wire can be soldered to conductive textile or conductive thread by low temperature solder paste. I used XGZ-Z40 conductive paste with the melting temperature 183°C. For soldering conductive thread is better to use the conductive paste with lower temperature. For example, FCT solder Sn42/Bi58 with temperature 138°C.



Fig. 4: Heating layer created by silver conductive thread.

#### V. CONCLUSION

The paper presents the concept of the intelligent set installed in the car or small airplane. The system is based on pressure, temperature and humidity sensors. The seat can be equipped by PID regulated heating system for increasing passenger comfort. The system is driven by MCU and data is transferred wirelessly to the central unit. Data are collected and it can be viewed by crew or service.

#### ACKNOWLEDGMENT

The described development has been supported by the Czech Ministry of Industry and Trade by the grant FV10087 Intelligent upholstery of vehicles. For simulations and experiments, equipment of the SIX Center was used (the grant LO1401). A partial support of Brno University of Technology is acknowledged (the grant FEKT-S-17- 4713).

#### REFERENCES

- [1] “Smart Textiles - Fundamentals, Design, and Interaction | Stefan Schneegass | Springer.” [Online]. Available: <https://www.springer.com/gp/book/9783319501239>. [Accessed: 04-Aug-2019].
- [2] “ATmega328P - 8-bit AVR Microcontrollers.” [Online]. Available: <https://www.microchip.com/wwwproducts/en/ATMEGA328P>. [Accessed: 04-Aug-2019].
- [3] “OWL253, OWS451,” *u-blox*, 17-Jul-2015. [Online]. Available: <https://www.u-blox.com/en/product/owl253-ows451>. [Accessed: 04-Aug-2019].
- [4] A. Torres, “International Centre for Numerical Methods in Engineering (CIMNE).” .

# Textile Integrated Waveguide Sensors for Smart Vehicle Interior Upholstery

Martin Kokolia

Department of Radio Electronics  
Brno University of Technology  
Brno, Czech Republic  
xkokol01@stud.feec.vutbr.cz

**Abstract**—This paper is proposing, textile substrate-integrated waveguide with two types of sensors that would utilize various SIW concepts that are useful for use in textile. Pressure sensor that could be used as interface button or as sensor of person presence is proposed first. Next the sensor of change of permittivity inside is proposed. This can simply sense humidity inside the textile or at higher frequencies could even sense smoke in the air with semi-open resonator configuration. Later conventional SIW with vias is to be replaced by more promising printable waveguides utilizing EBG cells as the artificial magnetic conductor

**Keywords**—Textile-integrated Waveguide, Sensor, Smart Vehicle, Humidity Detector, Smoke Detector, Pressure Detector

## I. INTRODUCTION

For past two decades there has been a strong trend to utilize microwave systems on textile substrate in both wearable application as well as upholstery textiles, mainly inside the means of transport. In those vehicles there is trend to introduce broad variety of smart systems to provide comfort or entertainment to passenger or to simply supplement need of conventional copper wires to connect already present components, such as sensor of LED light and such.

It is then convenient to use wireless power or signal transmission to save weight. If it is not possible for example to broadcast power supply or wide bandwidth due to obstacles or sensitive components in airplane, another possibility is to use waveguides inside textile.

Similar principle has been already presented in [1-4]. However, all those designs only worked as one type of sensor, which is given by use of special materials, capacitive sensing or antennas that senses its surrounding. Aim of this work is thus to propose extremely simple design that could be used as both of those sensors and be integrated into the textile substrate easily and cheaply.

## II. DESIGN OF THE FREQUENCY SELECTIVE SURFACE

For the best sensitivity of detectors using RB signal the highest possible frequency is useful. Considering limitations of technology and measurements of material [5,6] to be used which is 3D knitted textile 3D096 the chosen frequency band is 8 – 12 GHz. This band is quite used in practically used systems

of all kinds. Proposed 3D knitted textile is made of polypropylene in very organized structure that forms tightly knitted top and bottom with middle filling being formed by rows of fibers which keep distance while keeping the textile very much empty. This in combination with material used promises unusually low dielectric losses at microwave frequencies.

Basic idea of the proposed system is dual layer substrate integrated waveguide that consists of resonator cavity filter with stop-band frequency being shifted by sensed mechanical deformation of the resonance cavity or change of effective permittivity inside of the cavity. It is obvious that in case of sensor of humidity inside the textile or even smoke in air around the textile, the cavity must have some opening to let the sensed material inside. Of course, the more open cavity could more easily sense its surrounding, but the effectivity of the filter would diminish. The proposed design is shown below at Figs 1 and 2.

The resonator cavity is coupled to the main waveguide line by two slots perpendicular to the waveguide as shown at the Fig. 3. The length of the cavity on the top of the waveguide is such so at 10.5 GHz there are two halves of the wavelength and the wave is then coupled back to the waveguide on the slot on the other side. At each transition through the slot there is a phase shift and therefore at the other side two waves interfere with phase shift equal to 180 degrees.

In case of the smoke detector configuration, the slots at the top that allows the smoke to enter the cavity are placed in such way that the stationary wave at the cavity is forming the nod in the of the slots so they are not radiating energy outside are waveguide slot antenna.



As can be seen, the only difference between the pressure and smoke detector are slots in the top metallic layer and that the textile in between top and middle metallic layer is taken away to provide purely air-filled cavity. This way the sensitivity of the smoke detector is better as smoke would hardly propagate through the textile layer.

TABLE I. DIMENSIONS OF THE SENSOR

Symbol	Value	Unit
L1	37.00	mm
L2	10.00	mm
L3	11.50	mm
D1	3.00	mm
D2	12.75	mm
D3	0.70	mm
W1	1.00	mm
W2	0.70	mm

As shown, the proposed sensor is compact desing of only about 20x30 mm. The only disadvantage is need of two layers of textile. The proposed design consists of conventional SIW made of metallic vias and could be sawn by thin copper wire.

Fig. 1. Pressure detector, top – default stat, bottom – maximum deformation

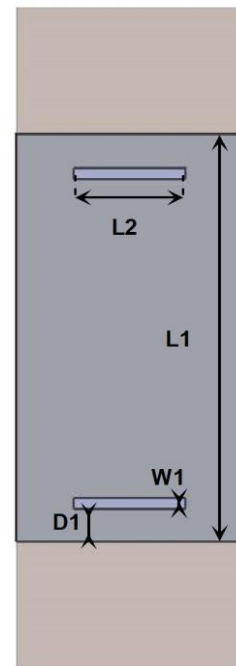
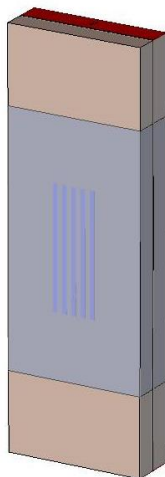


Fig. 2. Smoke and humidity detector

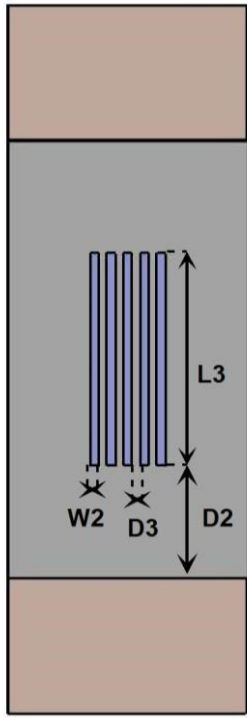


Fig. 3. Dimensions of the detector, top – middle metallic layer, bottom – top metallic layer of smoke detector

Later design could utilize other methods of forming waveguide like EBG cells forming artificial magnetic conductor as in previous work [7] and thus the design would be printable and simpler to manufacture.

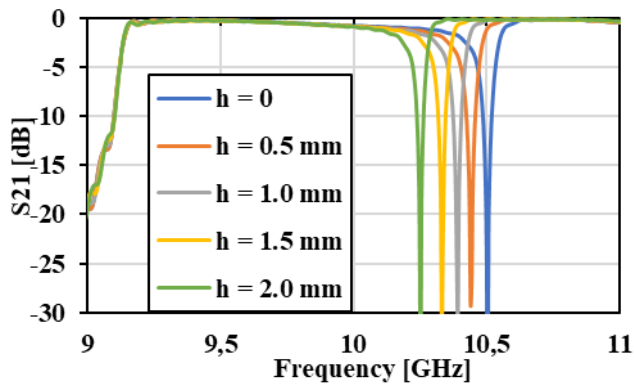


Fig. 4. Simulated dependence of the S21 on mechanical deformation of the sensor

As shown at the Fig. 3, in range of deformations that was practically tested as easily obtained, due to high quality factor of the resonance filter, the stop-band that is very narrow (about 1.5 %) is shifted for about 5 %. That is the core principle of the proposed systems. In practical application there would be constant signal at 10.5 GHz. In default state the filter would not allow the signal to pass through. Then if the sensor is pressed

enough, the signal can reach the receiving part of the system and the command that is represented by the button on the textile is executed by the system.

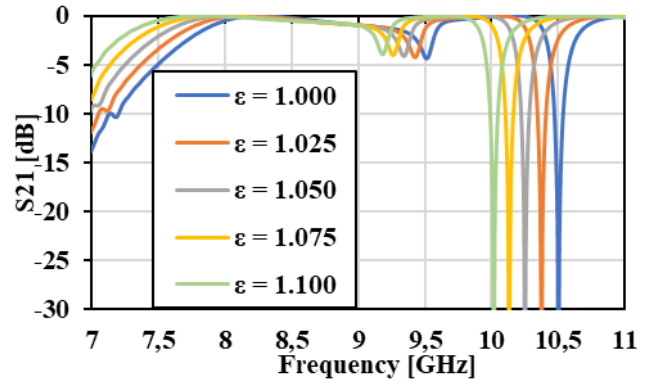


Fig. 5. Simulated dependence of the S21 on effective permittivity inside the sensor

As shown at the Fig. 4 even very slight change of the effective permittivity inside the cavity can cause significant enough change in the stop-band center frequency of the filter. This means that the proposed sensor can easily detect and after some calibration even roughly measure level of humidity inside the examined piece of the textile. Permittivity of the water at the room temperature is about 80, so even very low level will significantly change the stop-band center frequency. Therefore, with testing signal at several frequencies it would be possible to decide which frequency is not propagating through the sensor and then what is the level of humidity. Simulation shows expected results for detection of smoke. Results also show that there is enough detection range left for higher differences of relative permittivity in case of humidity detection.

In case of the smoke detector the sensitivity of the resonator cavity comes to use. As stated in [5] there are usually two types of smoke detectors (dominantly infrared and radioactive isotope) that each detect different type of smoke. First is for so-called white smoke and the latter for black smoke. White to gray smoke is formed by slow-smoldering fires with 0.5 – 10  $\mu\text{m}$  particles. In case of the black smoke the particles are smaller than 0.5  $\mu\text{m}$  and consist mainly of carbon which at 10 GHz band has permittivity roughly 2.3 [5]. Some conventional smoke detectors can sense as low as 200 ppm and more simple ones about 10000 ppm [6]. This lower level could obviously not be achieved, but according to the simulations and possible permittivity of the smoke particles the reasonable sensing threshold could be roughly 10000 to 20000 ppm which could be still used as cheap backup or non-critical option.

### III. CONCLUSION

The presented design was simulated with realistic materials and technology of manufacture taken in consideration. Results show that the sensor could be easily utilized as rough pressure detector or button controlling some function for user. Then the design was slightly altered to be used as sensor of surrounding permittivity which could detect and even roughly measure either humidity inside the textile or presence of smoke in the air. Design could be in future updated by EBG waveguide topology that would grant printability without need of sawing the SIW vias.

### ACKNOWLEDGMENT

The research was supported by the Czech Ministry of Education by the National Sustainability Program grant LO1401.

### REFERENCES

- [1] J. Lee, H. Kwon, J. Seo, S. Shin, J. hoon Koo, C. Pang, S. Son, J. hyung Kim, Y. hoon Jang, D. eun Kim, and T. Lee, "Conductive Fiber- Based Ultrasensitive Textile Pressure Sensor for Wearable Electronics", *Advanced Materials*, vol. 27, no. 15, pp. 2433-2439, 2015.
- [2] M. Mckeown, S. Julrat, S. Trabelsi, and E. Tollner, "Open Transverse-Slot Substrate-Integrated Waveguide Sensor for Biomass Permittivity Determination", *Ieee Transactions On Instrumentation And Measurement*, vol. 66, no. 8, pp. 2181-2188, 2017.
- [3] Y. Yun and H. Shin, "Simplified Structural Textile Respiration Sensor Based on Capacitive Pressure Sensing Method", *IEEE Sensors Journal*, vol. 14, no. 9, pp. 3245-3251, 2014.
- [4] W. Xu, M. -chun Huang, N. Amini, L. He, and M. Sarrafzadeh, "ECushion: A Textile Pressure Sensor Array Design and Calibration for Sitting Posture Analysis", *IEEE Sensors Journal*, vol. 13, no. 10, pp. 3926-3934, 2013.
- [5] KOKOLIA, Martin and Zbyněk RAIDA. Milimeter-wave Propagation in 3D Knitted Fabrics. 22nd International Microwave and Radar Conference. 2018.
- [6] M. Cupal; J. Dřinovský; T. Götthans; R. Hermany; M. Kokolia; J. Láčík; T. Pařízek; J. Prášek; Z. Raida; J. Špůrek; D. Kráčalová; Z. Lédrová; J. Procházka; D. Krutílek; Z. Řezníček; "Textile-integrated electronics for small airplanes," European Conference on Antennas and Propagation (EuCAP 2018), EurAAP, 2018.
- [7] KOKOLIA, M. Hexagonal-Cell Artificial Magnetic Conductor Waveguide. In *PROCEEDINGS OF 19TH International Conference on Microwave Techniques 2019*. 1. Pardubice: 2019. p. 24-28. ISBN: 978-1-5386-9336-0.
- [8] M. Hotta, M. Hayashi, M. Lanagan, D. Agrawal, K. Nagata, and M. Hotta, "Complex Permittivity of Graphite, Carbon Black and Coal Powders in the Ranges of X-band Frequencies (8.2 to 12.4 GHz) and between 1 and 10 GHz", *ISIJ International*, vol. 51, no. 11, pp. 1766-1772, 2011.
- [9] M. Vojtise,. "Assessment of Low Levels of Particulate Matter Exhaust Emissions Using Low-Cost Ionization-Type Smoke Detectors" [online]. In: . 2013-09-08, s. - [cit. 2019-08-15]. DOI: 10.4271/2013-24-0168. Dostupné z: <https://www.sae.org/content/2013-24-0168/>

# Improving of efficiency wireless charging

Josef Pokorny

Department of Theoretical and Experimental Electrical Engineering  
Brno University of Technology  
601 90 Brno, the Czech Republic  
xpokor61@vutbr.cz

**Abstract**— This article discusses how to improve the efficiency of Wireless Charging Stations (WCS). There is dismantled the tunnel magnetoresistance (TMR) sensor, which works on the basis of magnetic tunnel junction (MTJ). Further possibility of realization of active rectifier and replacement of sensing elements that save energy and increase efficiency of the device.

**Keywords**— *Wireless Charging Stations (WCS); magnetoresistance (TMR); active rectifier; Linear Current Sensor*

## I. INTRODUCTION

Today, wireless transmission is fading away, ahead of the innovative QC fast charging, PD protocol and powerful wire car chargers. Its advantage is air transmission up to tens of centimeters with efficiency over 90%. Wireless charging needs extra features to ensure the transfer itself, but also to use active features to increase efficiency. The main aspect of wireless transmission is the centering of the coils in the axis when the coils pass through the center and meet the edges, the transmission efficiency decreases rapidly. The charging power can be measured via mutual inductance, this requires measurement on both sides. Another way is to measure only on the receiving side, where based on empiricism we create an algorithm to center of the receiving side. Another way is to center the receiving coil by an automated system by means of motors. There is a method that can detect distance, misalignment, but also foreign objects in the wireless transmission area. TMR sensors have sensitivity in tens of mV/V/mT can be used for such sensing and visualize the current coil field by signal processing.[2] We cannot forget to use active elements in individual blocks for wireless transmission. Resistive current sensing shunts to measure the transferred power, or just the operation of integrated circuits, to replace monolithic current linear sensors that have tremendous efficiency and almost no loss. The entire block, which can also be replaced and saved, is a rectifier on the receiving side, just behind the receiving coil. An active rectifier can save power and increase frequency. The losses are dependent on the transient resistance and the excitation of the switching element. However, the problem arises with wake-up synchronization. [4]

## II. TMR UTILIZATION AND PRINCIPLE

This part describes the principle of TMR effect, which is created in magnetic tunnel junction (MTJ). In Figure 1, two magnets are connected by a thin insulator, by passing the

magnetic field electrons tunnel from one ferromagnet to the other. The rotation of the magnetic field can also be determined. The lower and upper contact is then sensed and can be sensed from the voltage element.



Fig. 1. TMR sensor structure.

If we assemble the matrix, then it is possible to sense a larger area, which is switched by matrix connection and converted by sensitive AD converters. The TMR sensor matrix in Figure 2 can be made on a printed circuit board, but it is necessary to include a change in the magnetic field when passing through the dielectric. The nut is placed on the receiving coil to be able to track the receiving field from the transmitting coil. [3]

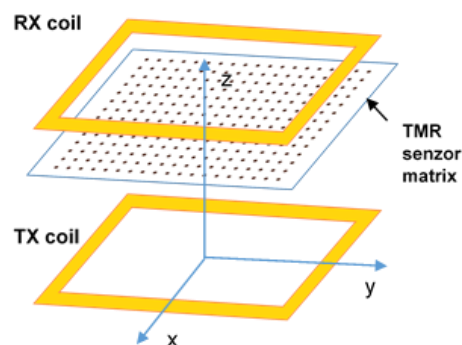


Fig. 2. TMR matrix location and coil layout.

The basic outline for improving efficiency and centering is shown in the block diagram in Figure 3. The charging station controls the charging and changes the frequency to fine tune the resonance. The range can vary (however, the most common use is the 20 ~ 200 kHz transmission coil). Transmitted magnetic field passes through TMR sensors that capture shape and intensity. The receiving coil drives an active rectifier from which the voltage for the batteries and the system controls is adjusted by means of converters. They also play an important role in pulse charging the battery pack, where the battery can be charged much faster when ordinary.

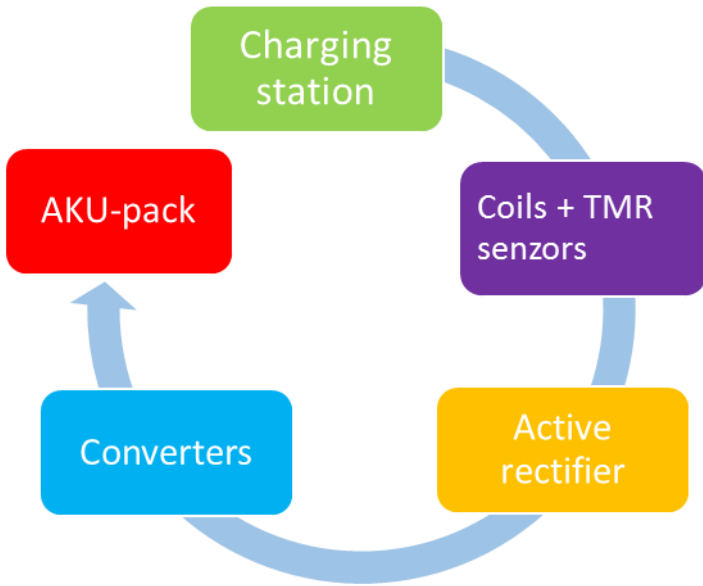


Fig. 3. WCS topology scheme.

### III. LINEAR CURRENT SENSOR

Great savings can be made by adding a Hall sensor (figure 4) that can be used in a DC-DC drive control station, detecting various devices, and detecting overcurrent in the circuit. The current flowing through the copper plate creates a magnetic field around the Hall probe, which converts it into a proportional voltage. The sensor can be used as uni- or bi- directional AC by DC sampler. With an internal resistance of  $100 \mu\Omega$ , provides low energy losses and survival in overcurrent conditions. [5]

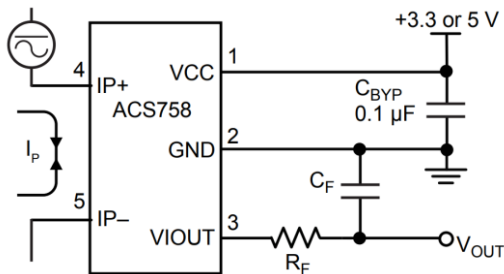


Fig. 4. The Hall sensor ACS758 outputs an analog signal. [5]

### IV. SIMULATION OF ACTIVE RECTIFIER

In Pspice was created circuit active rectifier shown in figure 5. The input Zener diodes with  $U_z = 3.9 \text{ V}$ , which allows only the trimmed voltage of 4.6 V from the receiving coil, which is supplied to the terminals of the comparator LM319. The flip-over levels are set by means of voltage sources so that the comparator outputs flip over at a voltage difference of 0.2V. The comparator outputs are fed to the XOR 7402 gate, which provide a guard interval using an MKO created with R10, C1, U3B and U4B.

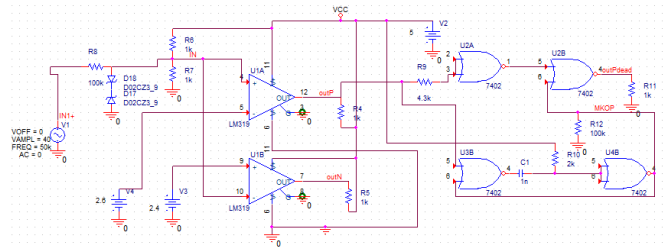


Fig. 5. Simulated input part of active rectifier.

In Fig. 6 we can notice the input voltage  $IN1$  and the output waveforms  $outN$  and  $outP$  from the comparator that will switch the gate of the transistors.  $OutPdead$  protection interval is created for  $outP$  course, which is created by MKO (yellow course).

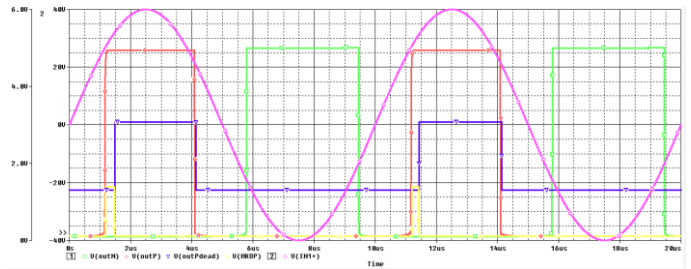


Fig. 6. Voltage waveforms for switching H bridge Realization of rectifier

### V. DESIGN AND MEASURING OF RECTIFIER

Active rectifier is solved by H bridge, which is connected directly to the receiving coil. The bridge is controlled by the dual comparator LM319. The circuit has low offset voltage, fast run time and a maximum power supply of  $\pm 15 \text{ V}$ . [1] From the comparator, the transistors are controlled via an optocoupler. The switching delay of the optocoupler is a maximum of 6 ns and thus the optocoupler sufficiently replaces, together with the gate comparator 7402, at the same time separating the AC and DC signal ground. Power supply for comparator and optocoupler is solved by Zener diode with voltage  $U_z = 5 \text{ V}$ . Symmetrical input  $\pm 2,5 \text{ V}$  to comparator is formed by resistors R15 and R16. The flip-over voltage level is then generated by the resistors R17, R18 and R19 by equation (1) and equation (2).

$$u_{komp+} = \frac{u_z}{2} + 2,5 - \frac{U_{cc}}{R17+R18+R19} \cdot (R18 + R19) \quad (1)$$

$$u_{komp-} = -\frac{u_z}{2} + 2,5 + \frac{U_{cc}}{R17+R18+R19} \cdot R19 \quad (2)$$

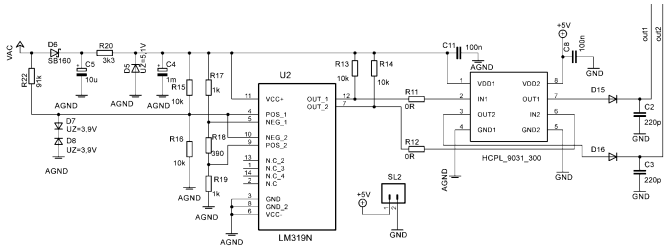


Fig. 7. The input part of the active rectifier.

From the optocoupler outputs in Figure 7, a galvanically isolated signal is output through the Schottky diodes D15 and D16, which prevent reverse currents and optocoupler interference. The signals are applied to the UCC27714 drivers, which are also used for the transducer-side inverter. The IRF3205S mosfets then rectify the voltage from the coil that is applied to the terminals via a DC / DC converter and regulated to the appropriate battery voltage. The manufacturer indicates the transistor resistance in the closed state  $R_{dsON} = 8 \text{ m}\Omega$ . Of course, these are ideal losses and neglected ambient influences and switching losses, but this is a significant difference compared to a conventional rectifier.

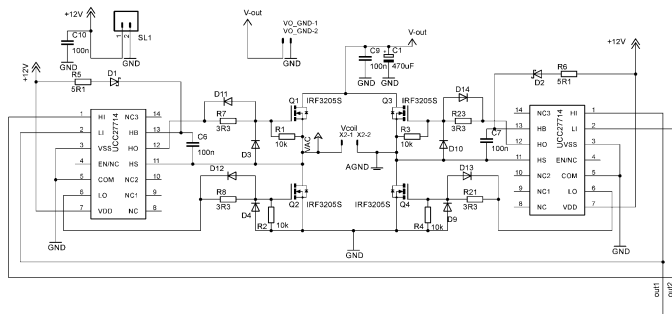


Fig. 8. Control circuits and power part of active rectifier.

Although the active rectifier senses the voltage from the receiving coil and the comparator flips over the set voltage values, 100% functionality has not been achieved after many experiments. In Figure 9, the output signals from the comparator can be observed. It can be seen from the signals that the voltage is cut from above to a maximum level of 5 V, however, as the edge descends, there are negative spikes. Despite the galvanic isolation of the optocoupler, the drivers for Mosfets could not be

switched correctly. The device worked up to a power transmission of 5 W, which is a fraction of the required power. At higher performances it stopped reliably rectifying.



Fig. 9. Measurement of LM319 comparator outputs.

## VI. CONCLUSION

The aim of this work is to open up new possibilities for wireless charging development. TMR sensors are potentially useful for the correct centering of the wireless system, for example for vehicles and small flying objects. They also contribute to the detection of foreign bodies in the wireless transmission area. Linear current sensor has up to 2 orders of magnitude less resistivity than ordinary short circuits. The possibility of active rectification by means of the H-bridge was investigated. However, the rectifier did not operate reliably at higher power levels. A better topology and a clearer signal received by the Rx coil are necessary for proper rectification.

## REFERENCES

- [1] LMx19 High Speed Dual Comparator [online]. 2017 [cit. 2019-05-26]. Web: <http://www.ti.com/lit/ds/symlink/lm319-n.pdf>
- [2] N. Kuyvenhoven, C. Dean, J. Melton et al., "Development of a foreign object detection and analysis method for wireless power systems." in Proc. IEEE Symp. Product Compliance Eng. (PSES), Oct. 2011, pp. 1-6.
- [3] Huaiqing Zhang, Feifan Li, Huan Guo, Zhiyuan Yang, Nian Yu, "Current Measurement With 3-D Coreless TMR Sensor Array for Inclined Conductor", Sensors Journal IEEE, vol. 19, no. 16, pp. 6684-6690, 2019. K. Elissa, "Title of paper if known," unpublished.
- [4] T. Kan, F. Lu, T. Nguyen, P. P. Mercier and C. C. Mi, "Integrated Coil Design for EV Wireless Charging Systems Using LCC Compensation Topology," in IEEE Transactions on Power Electronics, vol. 33, no. 11, pp. 9231-9241, Nov. 2018.
- [5] M. ACS758 – Hall Effect-Based linear Current Sensor IC [online]. 2017 [cit. 2019-06-12]. Web: <https://datasheet.octopart.com/ACS758ECB-200B-PFF-T-Allegro-datasheet-10031246.pdf>

# Watershed Segmentation for Peak Picking of High-Resolution Mass Spectrometry Data

Vojtech Barton, Helena Skutkova  
Department of Biomedical Engineering  
Brno University of Technology  
Email: barton@vutbr.cz, skutkova@vutbr.cz

**Abstract**—We are presenting the approach to process different resolution gas chromatography-mass spectrometry data. We are aiming to identify the peaks in the data that can be used in other tools to process the experiment data. Our approach is using a known image processing method, bypassing traditional scan-by-scan approach.

## I. INTRODUCTION

Mass spectrometry with gas chromatography is an analytical method used to identify and quantify chemical compounds in the sample. It is widely used in environmental studies, medical sciences and forensic. The modern instruments like orbitrap are using ion traps, and Fourier transforms to determine the intensity of measured peaks. [1]

This computational instrument method allows measuring in high resolution of above ten decimal places. This is making the requirements to adapt the algorithm to process large amounts of data and databases to compare spectra of known compounds. [2]

The biggest challenge is to process untargeted experiments. This type of experiment is used for screening purposes. It could be widely used in environmental screening to study the complex impact of pollution in the environment. [3]

Using this type of experiment, it emerges the need to process complex samples of unknown compounds. Also, it is raising the needs to process the samples from acquisition to compounds identification automatically. It involves steps like data filtration, peak identification, deconvolution, ion, and compounds identification. Most of these steps are right now carried by signal processing methods and working by scans. [4] [5]

One of the bottlenecks of the algorithms is the volume of the data and a need to internally align the scans to have the same values for the same ions. This can be solved by using some image processing methods, which raised the need to align the scans onto the defined grid. [6]

Mass spectrometry imaging [7] is a known method, but using image processing algorithms in gas chromatography-mass spectrometry (GC-MS) is relatively new.

## II. PROCESSING

The raw data contain the information about the acquisition, and the data points represented as a three-values vector of their retention time, mass to charge ratio, and intensity. We convert the raw format into a csv file with three columns.

### A. Data

For testing puprose we were working with a set of gas chromatography-mass spectrometry experiments measured at Orbitrap instrument with settings producing profile data.

The data are organized as a 2D array with coordinates in rt and mz axis and the value represented as the intensity of the signal. As such we could form an image-like array. Intensity values are represented in double format. Retention time can be expressed in seconds, or integers of the ordering of the scans. MZ axis depends on the required precision.

With the first inspection of the data, we could see some zero intensity points. Also, retention time vector in seconds is not equally sampled. The differences between consecutive scans are shown in figure 1.

MZ vector also does not contain equally sampled points in all of the scans.

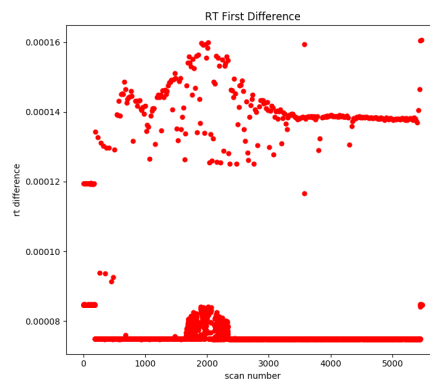


Fig. 1. RT difference

### B. Preprocessing

To apply some known image processing methods, we first need to construct the data matrix with an equally sampled axis. We can use the numbers of the scans instead of their time values as the differences are small, and their impact on the resolution of the method is marginal.

With the vector of the mz values, we need resampling. The sampling frequency of the new vector will determine the required precision of the measurement. We tested linear resampling and b-spline. We decided to use linear interpolation

as the b-spline method produce artifacts at the borders of the peaks as shown in figure 2.

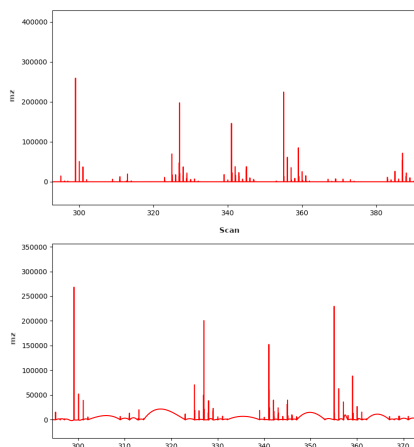


Fig. 2. Interpolation of scans. (Top - linear, bottom - b-spline)

After the zero intensity values removal, and resampling of the scans with the desired precision, we can construct the data matrix with stacking the scans consecutively as the columns of the matrix. To decrease the memory demands, we convert the data matrix to sparse matrices format as the matrix contain non-zero data only in quite narrow peaks areas widely spread across the matrix. The example of the matrix is shown in figure 3.

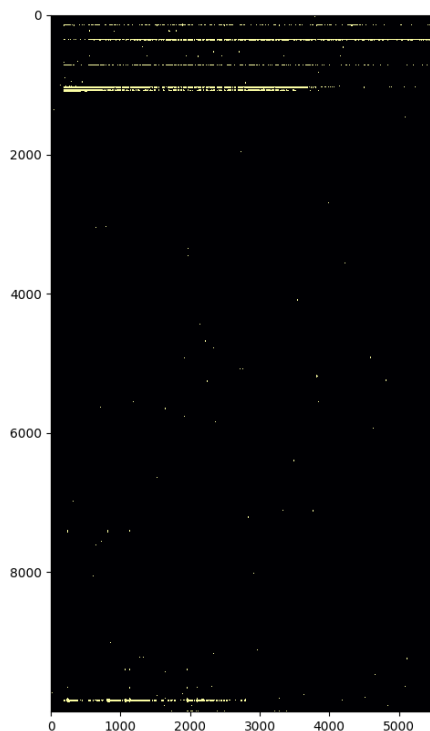


Fig. 3. Datamatrix of the experiment.

### C. ROIs

We use the algorithm described above to identify the regions of interest in the data matrix. We define the ROI as a connected set of points representing mass spectrometry peak, ideally with only one maximum.

To identify the ROIs, we will be applying the watershed algorithm. Firstly we convert our matrix to the binary array. Then we compute the distance matrix of the mask produced from the previous step. We decided to use euclidean distance metric.

From the distance image, we obtain local maxima to be used as input to the marker-based watershed algorithm. Then we label the regions by the watershed algorithm from distance image and identify markers.

Produced regions are then used as a mask, applicable to the original image, to obtain the data from one region.

### D. Peak picking

To be able to work in high resolution, we will be applying the method in two steps. Firstly we resample with the precision equal to two decimal places and create a data matrix. Every identified region is then extracted and resampled again from original data, but with higher precision depending on require precision. From the new high-resolution data, we obtain the region of interests, as described above.

We consider every ROI as one peak area. From every ROI, we identify the selected features. We compute the coordinates of the center of mass, local maximum position, and intensity, peak area, and eccentricity. As a peak location, the analyst can use the maximum or center of the mass. Peak area is essential for further quantization and identification of the chemical compound. The eccentricity is then used to filter non-standard peaks, as all the peaks should be somewhat elliptic in the  $rt$ - $m/z$  domain. The example of the identified peak is shown in figure 4. The bottom image is showing the data matrix of selected ROI and the top image showing the total ion current of the area.

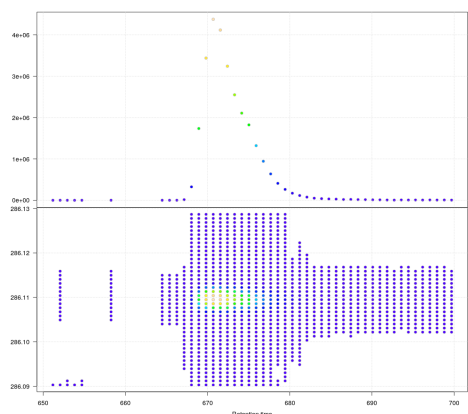


Fig. 4. Detail of one of identified ROI.

## III. DISCUSSION

Presented algorithm for processing the data are dealing with a two main problem of spectrometric data obtained from

high-resolution orbitrap system. First is the non-equality of the sampling rate. This can be dealt with by resampling the data to the equally distant grid.

The second problem is the volume of the data. This is overcome by using a sparse matrix data format for storing the experiment data, and then dividing the data to regions in low resolution and then using the high resolution only in the small identified areas to precisely identify the features.

Nevertheless, the peak picking step is only one step in the whole complex mass spectrometry data processing pipelines, including further steps like peaks deconvolution, identification, quantization, and more, depending on the chosen tool. Most of the tools are working by scans, with signal processing methods. The hands of the analyst still hold most of the work in processing GC-MS data. Such as there are emerging many tools to automatize this process. [8]

Our presented algorithm will still be needed to test on the complex samples to determine the right parameters, but as such, it is designed to be easily incorporated into the existing pipelines, representing only one of the complex tasks series. [9]

#### IV. CONCLUSION

We are presenting the workflow of possible data processing in high-resolution mass spectrometry. Our simple image processing approach can identify the peaks and their features, bypassing the traditional signal processing methods and the need for spectra alignment and their post-processing. Our peaks identified as a three-element vector of the *rt*, *mz* and intensity value can be easily adapted to be used in other known tools for mass spectrometry processing to deconvolve the spectra and identify and quantify the compounds.

Our approach is also adaptable to different *mz* precision needs, which means that it could work both on data obtained from low and high-resolution instruments. Also by working with different precision scale in selected areas, we are reducing the computational demands to process the experiments, which could be a real bottleneck in processing large experiments.

#### ACKNOWLEDGMENT

Computational resources were provided by the CESNET LM2015042 and the CERIT Scientific Cloud LM2015085, provided under the programme "Projects of Large Research, Development, and Innovations Infrastructures".

This work was supported by grant project of the Czech Science Foundation [GACR 17-01821S].

#### REFERENCES

- [1] R. A. Zubarev and A. Makarov, "Orbitrap Mass Spectrometry," *Analytical Chemistry*, vol. 85, no. 11, pp. 5288–5296, jun 2013. [Online]. Available: <http://pubs.acs.org/doi/10.1021/ac4001223>
- [2] C. Kuhl, R. Tautenhahn, C. Böttcher, T. R. Larson, and S. Neumann, "CAMERA: An integrated strategy for compound spectra extraction and annotation of LC/MS data sets." *Analytical Chemistry*, 2011. [Online]. Available: <http://www.ncbi.nlm.nih.gov/pubmed/22111785>
- [3] R. Tautenhahn, G. J. Patti, D. Rinehart, and G. Siuzdak, "XCMS online: A web-based platform to process untargeted metabolomic data," *Analytical Chemistry*, vol. 84, no. 11, pp. 5035–5039, 2012.
- [4] L. G. Johnsen, P. B. Skou, B. Khakimov, and R. Bro, "Gas chromatography mass spectrometry data processing made easy," *Journal of Chromatography A*, vol. 1503, pp. 57–64, 2017. [Online]. Available: <http://dx.doi.org/10.1016/j.chroma.2017.04.052>
- [5] Y.-M. Zhang, Y.-Y. Zhang, Q. Zhang, Y. Lv, T. Sun, L. Han, C.-C. Bai, and Y.-J. Yu, "Automatic peak detection coupled with multivariate curve resolution/alternating least squares for peak resolution in gas chromatography/mass spectrometry," *Journal of Chromatography A*, vol. 1601, pp. 300–309, sep 2019. [Online]. Available: <https://www.sciencedirect.com/science/article/pii/S0021967319304509?via=ihub>
- [6] V. Treviño, I. L. Yañez-Garza, C. E. Rodríguez-López, R. Urrea-López, M. L. Garza-Rodríguez, H. A. Barrera-Saldaña, J. G. Tamez-Peña, R. Winkler, and R. I. Díaz De-La-Garza, "GridMass: A fast two-dimensional feature detection method for LC/MS," *Journal of Mass Spectrometry*, vol. 50, no. 1, pp. 165–174, 2015.
- [7] J. He, L. Huang, R. Tian, T. Li, C. Sun, X. Song, Y. Lv, Z. Luo, X. Li, and Z. Abliz, "MassImager: A software for interactive and in-depth analysis of mass spectrometry imaging data," *Analytica Chimica Acta*, vol. 1015, pp. 50–57, jul 2018. [Online]. Available: <https://www.sciencedirect.com/science/article/pii/S0003267018302459>
- [8] Y. Ni, Y. Qiu, W. Jiang, K. Suttlemyre, M. Su, W. Zhang, W. Jia, and X. Du, "ADAP-GC 2.0: Deconvolution of coeluting metabolites from GC/TOF-MS data for metabolomics studies," *Analytical Chemistry*, vol. 84, no. 15, pp. 6619–6629, 2012.
- [9] D. D. Naturwissenschaften, "OpenMS A framework for computational mass spectrometry," 2010.

# Crest Factor Reduction and Digital Predistortion under Nonlinear Power Amplifier

Jakub Gotthans, Roman Maršálek and Tomáš Gotthans

Department of Radio Electronics, Brno University of Technology, 616 00 Brno, Czech Republic

**Abstract**—The adaptive digital predistortion is currently widely used to compensate for the non-linearities. However, due to natural properties of transmitted signal e.g. high peak to average ratio, the efficiency of transmission decreases. In this paper we would like to show impact of combination of Crest Factor Reduction method with Digital Predistortion under Nonlinear Power Amplifier using Quadrature Amplitude Modulation or Orthogonal Frequency Division Multiplexing. For the evaluation of methods will be used Peak-to-Average Power Ratio, Error Vector Magnitude, and Normalized Mean-Squared Error.

## I. INTRODUCTION

Efficiency and linearity are usually the two most important parameters of power amplifiers (PA). To maximize efficiency that is important for energy savings in the overall system, PAs must be operated close to saturation. However, PAs in this area usually show strong nonlinear behavior. The combination of Crest Factor (CF) and Digital Predistortion (DPD) allows to improve Power Amplifier efficiency which leads to higher integration of hardware and lower power consumption. The CF is defined as the peak amplitude of the waveform divided by the RMS value of the waveform. The high Peak-to-Average Power Ratio (PAPR) is problematic for most of the modulation methods that are currently used. For example OFDM used in 4G networks, is using large number of independent signals, which cause high CF in signal. In paper [1] experimental results show that at system level the CFR techniques can reasonably reduce the PAPR of the input signals. However, to comply with the stringent requirements of the modern communication standards, the linearization techniques need to be more efficient to constrain the Out-Of-Band (OOB) radiations generated by used CFR technique.

### A. Power Amplifier Models

Saleh's nonlinear model was first presented in [2] and has found popular use in the behavioral modeling of modern RF nonlinear PAs. However, it has been assumed that the PA is memoryless usually only over a narrowband [3]. The model was originally presented for traveling wave tube amplifiers (TWTAs). Nowadays, most of the TWTAs has been replaced with solid states power amplifiers (SSPA), where the main modeling difference can be lower phase deviation. Nevertheless, the Saleh model is still valid due to it's simplicity. Original 4-parameter generic model with phase extension (AM-PM), applicable in either polar or quadrature form, is:

$$y_{AM}(x) = \frac{\alpha_{AM} x^n}{1 + \beta_{AM} x^2}{}^v; y_{\Phi}(x) = \frac{\alpha_{\Phi} x^2}{1 + \beta_{\Phi} x^2}, \quad (1)$$

where  $n = 1, 2$  or  $3$  and  $v = 1$  or  $2$ , approximating coefficients  $\alpha$  and  $\beta$ , may be extracted using least squares (LS) approximation [3].

### B. Digital Predistortion

The interest of DPD using memory polynomials [4] is that we can obtain a convex minimization problem for the least-squares (LS) criteria for DPD coefficients calculation with indirect learning architecture. The problem can be written:

$$\mathbf{x} = \mathbf{U}\mathbf{b}. \quad (2)$$

Where  $\mathbf{x}$  is data vector,  $\mathbf{b}$  are coefficients and  $\mathbf{U}$  is a matrix of size  $N \times N_c$  (where  $N$  is number of samples and  $N_c$  represents number of coefficients). The overall model structure determined by 2 parameters: the non-linearity order  $K$  and the memory length  $M$ . The output of memory polynomial series can be expressed as follows:

$$\begin{aligned} z(n) &= \sum_{k=1}^K \sum_{m=0}^M b_{km} x(n-m)|x(n-m)|^{k-1} \\ &= \mathbf{U}(n)\mathbf{b}. \end{aligned} \quad (3)$$

### C. Crest Factor Reduction

The crest factor of a signal is defined as the ratio between peak amplitude input and its root mean square (RMS) value:

$$C = \frac{|x|_{peak}}{x_{rms}}. \quad (4)$$

CFR is a technique used to reduce the PAPR of the transmitted signals to achieve higher efficiency of PA.

#### 1) Clipping:

$$x_{clip}(n) = c(n)x(n), c(n) = \begin{cases} \frac{A}{|x(n)|} & |x(n)| \geq A \\ 1 & |x(n)| < A, \end{cases} \quad (5)$$

where  $A$  is desired amplitude,  $x(n)$  is the input signal,  $c(n)$  is the clipping algorithm here. Clipping can cause sharp corners in a clipped signal, which lead to an unwanted OOB emission (increased ACPR). Moreover to reduce the unwanted OOB emissions, the clipped signal can then go through a low-pass filter to reduce the high frequency signals which correspond to the sharp corners in the clipped signal.

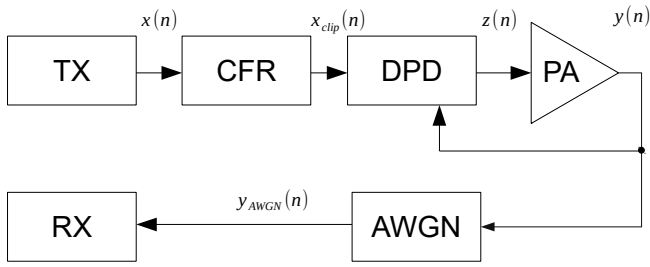


Fig. 1. Proposed simulation schematics, where CFR stands for crest factor reduction and DPD for digital predistortion.

## II. SIMULATION

### A. Figure of Merits

In order to evaluate contribution of presented method, important measures need to be defined.

#### 1) Peak to Average Power Ratio - PAPR:

$$PAPR = \frac{|x|_{peak}^2}{x_{rms}^2} = C^2. \quad (6)$$

Usually the PAPR is expressed in decibels (dB). The knowledge of PAPR is important, because it is a measure of the envelope dynamics.

2) *Adjacent Channel Power Ration - ACPR*: The imperfections and non-linearities usually result in some adjacent channel spectral regrowth. This phenomenon can be quantified with the parameter ACPR that is defined as a bandwidth limited ratio between the power in the main channel and the power in one adjacent channel. Therefore we can define this property for left and right adjacent channel. The right (by changing the boundaries for left) channel ACPR is defined by:

$$ACPR_R[dB] = 10 \log \left( \frac{\int_{-B/2}^{B/2} P_y(f) df}{\int_{B/2}^{3B/2} P_y(f) df} \right) \quad (7)$$

where  $B$  represents the bandwidth of the signal and  $P_y(f)$  is power spectral density.

3) *Normalized Mean Square Error - NMSE*: For the quantification of performance we can also use Normalized Mean Square Error (NMSE)[?]. It is an estimator of the overall deviations between predicted and measured values. For two complex vectors  $\mathbf{x}$  and  $\mathbf{y}$  of  $N$  samples the NMSE is defined as:

$$NMSE(\mathbf{x}, \mathbf{y})[dB] = 10 \log \left( \frac{(\mathbf{x} - \mathbf{y})^H (\mathbf{x} - \mathbf{y})}{\mathbf{x}^H \mathbf{x}} \right). \quad (8)$$

Where  $(\cdot)^H$  stands for transposed complex conjugation of vector also so-called Hermitian transpose.

The NMSE is a global measure of quality. But it does not distinguish between linear and non-linear distortion.

For example bad NMSE could be caused due to time shift between signals and/or bad gain alignment.

4) *Error Vector Magnitude - EVM*: Error vector magnitude (EVM) is a measurement of performance in the presence of impairments. The measured symbol location obtained after decimating the recovered waveform at the demodulator output are compared with the ideal symbol locations of constellation points. The EVM is defined as normalized average value of the vector error. It is usually estimated on a window of  $N$  samples. The measured symbol location is given by  $w$ . However, the ideal symbol location (using the symbol map) is given by  $v$ . Therefore, the resulting error vector is the difference between the actual measured and ideal symbol vectors defined as  $e = w - v$ .

The EVM is calculated after compensation of simple constellation determination: offset and complex gain. Analytically, RMS EVM is defined as:

$$EVM = \frac{E(|v - c_1 w - c_0|^2)}{E(|v|^2)}, \quad (9)$$

where  $E(\cdot)$  represents the average value,  $c_0$  and  $c_1$  are the optimal values of gain and offset. Using ergodic properties, it is estimated on  $N$  symbols by (in the case where  $c_0 = 0$  and  $c_1 = 1$ ):

$$EVM = \frac{\sum_{j=1}^N [(I_j - I_j^{meas})^2 + (Q_j - Q_j^{meas})^2]}{\sum_{j=1}^N |I_j^2 + Q_j^2|} 100\%. \quad (10)$$

5) *Input Back-Off Level - IBO*: One way dealing with the effects of the nonlinear region of PA we can lower the operating point of the PA via a suitable input back-off (IBO) level denoted as  $\gamma^2$  defined in [5] as:

$$\gamma^2[dB] = 10 \log \left( \frac{A_{sat}^2}{P_{in}} \right) = 10 \log \left( \frac{A_{sat}^2}{\mathbb{E}\{|x(n)|^2\}} \right) \quad (11)$$

The IBO level  $\gamma^2$  is defined as the quotient point of the amplifier saturation power ( $A_{sat}^2$ ) and the input signal mean power ( $P_{in}$ ).

## III. RESULTS

The simulation was setup as shown in Fig. 1. The transmitter (TX) is 16-QAM generator with Root-Raised Cosine filter (roll-off  $\alpha = 0.15$  and span  $\beta = 80$  symbols) and oversampling ratio 5. For each simulation a block of 614400 samples was generated. The transmitter is feeding symbols to CRF block capable of reducing PAPR, related with ACPR regrowth (Fig. 5) and NMSE degradation (Fig. 4). As a digital predistorter a memory-less polynomials (we use memory-less Saleh power amplifier model) have been used (see eq. (3) with non-linear order  $K = 7$ ). The results clearly demonstrate that the CFR (clipping based - see eq. (5)) reduces PAPR significantly with a cost of NMSE and ACPR degradation. Using digital predistorter the performance can be improved. Overall using CDR and DPD leads to PA efficiency improvement, since the quiescent point can be shifted towards saturation.

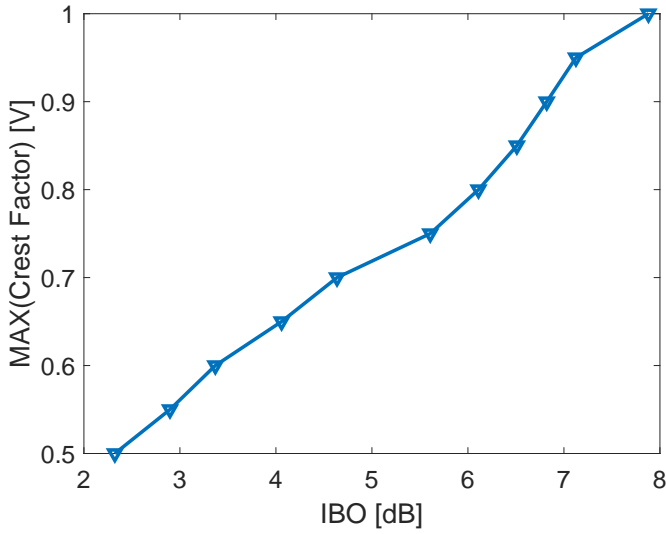


Fig. 2. Dependency of maximum crest factor value on Input-back-off (IBO).

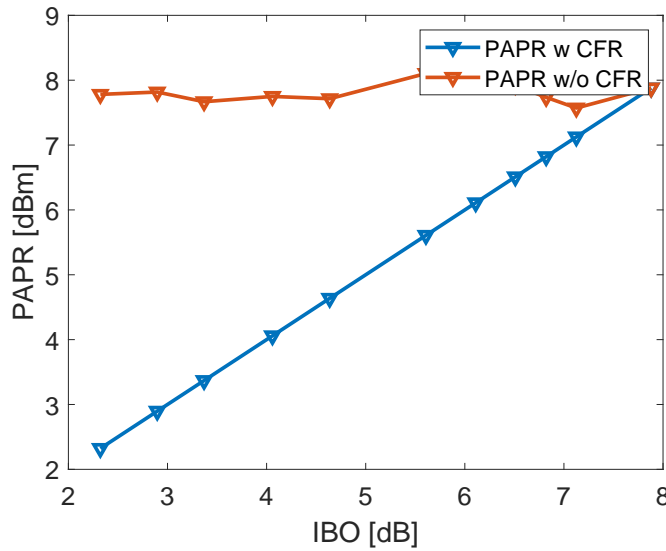


Fig. 3. Dependency of Peak to average power ratio (PAPR) on Input-back-off (IBO). Red curve denotes PAPR without Crest factor reduction (CFR), whilst the blue curve shows PAPR dependency with CFR.

#### IV. CONCLUSION

In this paper, we introduced the possibility of increasing efficiency and improving linearity of transmission. First we have used crest factor reduction reducing PAPR (therefore allowing the quiescent point of PA to be increased) leading to increase of OOB emissions. The CFR was followed by digital predistorter capable reducing the nonlinear effects and decreasing energy out of band. The proposed idea was evaluated using simulations. The simulations clearly showed improvement (e.g. for IBO= 2.2 dB the output of PAs ACPR with CFR is -18 dBm and with DPD it improves to -28 dBm, where the NMSE improves 22dB).

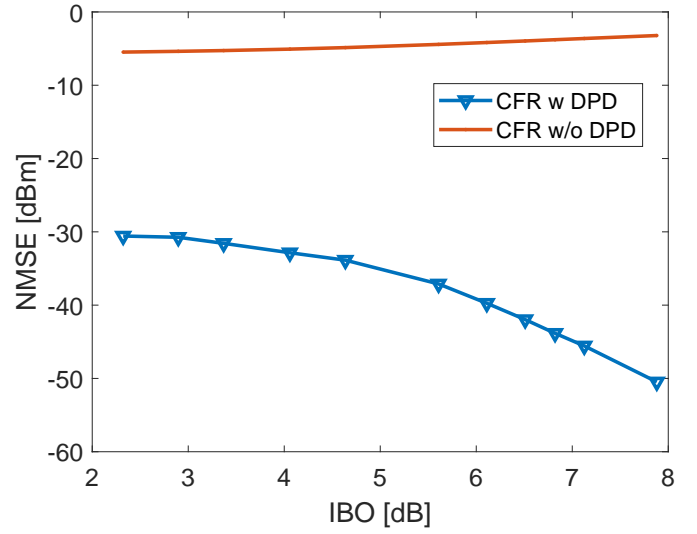


Fig. 4. Proposed simulation schematics, where CFR stands for crest factor reduction and DPD for digital predistortion.

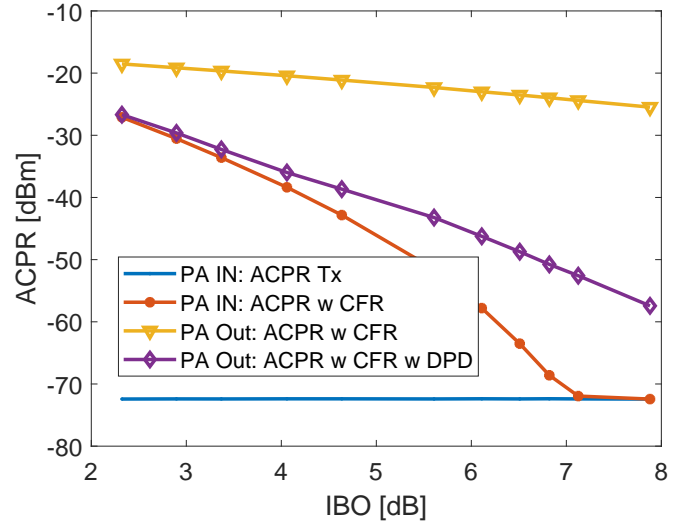


Fig. 5. Proposed simulation schematics, where CFR stands for crest factor reduction and DPD for digital predistortion.

#### ACKNOWLEDGMENT

Research described in this paper was financed by Czech Science Foundation project 17-18675S *Future transceiver techniques for the society in motion* and partially supported by the Czech Ministry of Education in frame of National Sustainability Program under grant LO1401. For research, infrastructure of the SIX Center was used.

#### REFERENCES

- [1] M. V. DeepakNair, R. Giofr, L. Piazzon, P. Colantonio, and F. M. Ghanouchi, "Effects of windowing based crest factor reduction technique on digitally predistorted pas for multicarrier wcdma," in *2015 IEEE International Wireless Symposium (IWS 2015)*, March 2015, pp. 1–4.
- [2] A. A. M. Saleh, "Frequency-independent and frequency-dependent nonlinear models of twt amplifiers," *IEEE Transactions on Communications*, vol. 29, no. 11, pp. 1715–1720, November 1981.

- [3] M. O'Droma, S. Meza, and Y. Lei, "New modified saleh models for memoryless nonlinear power amplifier behavioural modelling," *IEEE Communications Letters*, vol. 13, no. 6, pp. 399–401, June 2009.
- [4] R. Raich, Hua Qian, and G. T. Zhou, "Orthogonal polynomials for power amplifier modeling and predistorter design," *IEEE Transactions on Vehicular Technology*, vol. 53, no. 5, pp. 1468–1479, Sep. 2004.
- [5] S. C. Thompson, J. G. Proakis, and J. R. Zeidler, "The effectiveness of signal clipping for papr and total degradation reduction in ofdm systems," in *GLOBECOM '05. IEEE Global Telecommunications Conference, 2005.*, vol. 5, Nov 2005, pp. 5 pp.–2811.

# Multiplatform System for Hand Gesture Recognition

Tomáš Bravenec

Department of Radio Electronics  
Brno University of Technology  
Brno, Czech Republic  
xbrave01@vutbr.cz

**Abstract**—This paper is focused on hand gestures and finger detection in still images and video sequences. The paper also contains a summary of different approaches to hand gesture detections as well as the realization of the platform independent application written in Python using OpenCV and PyTorch libraries, that can show a selected image or play a video sequence with highlighted recognized gestures.

**Keywords**—Hand detection, Gesture recognition, Deep Learning

## I. INTRODUCTION

For quite some time, the field of computer vision is rising in popularity. Nowadays computers and smart phones are powerful enough to analyze images and video sequences in real time. For example, our mobile phones are in most cases capable of recognizing our faces in photos and sometimes they can even understand some basic hand gestures for taking a picture without us even touching the phone. Computers are quite capable of these easy recognitions when they can see the whole face or hand, but what about cases when hands and fingers are not visible that well? This is quite an issue that is not that easy to handle.

Analysis of hand gestures is useful for providing another way of understanding what humans are doing in videos for visually impaired or blind people or translation of sign language to text. Another example could be gesture based controls of some systems in automotive industry, to analyze non-verbal communication of criminals caught on cameras etc.

## II. HANDS DETECTION

To begin with gesture recognition, the hand must be first detected within a picture frame. There are several approaches to finding the hand with different complexity and success rate.

### A. Contour Analysis

From a thresholded image (see Fig. 1a), it is easy to get the contour of a hand and convex hull around the hand if the hand is easily separable from the background [1]. Apart from thresholding, the separation could be done by skin color, background subtraction etc. The disadvantage is the algorithm can become easily confused when it comes to unusual background patterns or just a sharp change in light.

### B. Curve fitting

Curve fitting, also known as snakes, is one of the less usable methods for hand detection. This approach needs some initial guess or cooperation from the person using this method [2]. The initial guess could be made by the person matching the curve on screen with his hand (see Fig. 1b). Because of this, the method is not a very good choice for detection in existing video sequences.

### C. Model Fitting

Another approach is creating a virtual model of a hand (see Fig. 1c), composed from *bones* and *joints* like in a real hand [3]. It uses contour analysis or depth image analysis, followed by connecting detected fingertips to the model, so the model joints can bend and recreate the gesture in a virtual environment. The problem here is again, that from certain angles, the model may not be properly connected to fingertips, which will cause unpredictable behavior, like guessing an incorrect gesture or losing focus on the hand itself [4].

### D. Depth Based Method

Another way of detecting hands rather in real time is based on capturing not only color but also depth (see Fig. 1d). This can be done using special capturing devices such as Microsoft Kinect. Here, the depth levels have lower resolution than color, which means that like a hand will mostly be on one or two neighboring distance layers, making hand detection significantly easier than from a color image. The advantage of depth approach is an independence to background or lighting conditions [5].

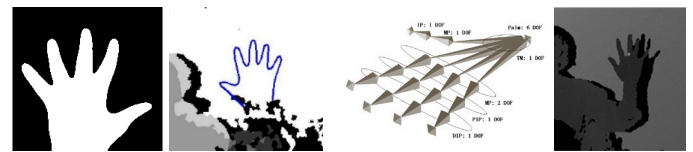


Fig. 1. Hand detection methods: a) Contour analysis, b) Curve fitting, c) Model fitting, d) Depth capture.

### E. Deep Learning

In the last couple of years, the field of machine learning started to gain in popularity, as the main limitation in the past, the processing power, is more accessible than ever before. The deep learning itself is a subset of machine learning, that today makes use mostly of deep neural networks (these networks

contain more than two layers of non-linear processing between input and output layers) to learn from huge amounts of data to solve problems without being explicitly programmed to do so.

Before training a neural network, there must exist some data to train the network on. There are several existing datasets and data sources which could be used for the purpose of hand detection, such as Oxford hands dataset [6], EgoHands dataset [7], New Zealand Sign Language Dictionary [8], MPII Human pose estimation dataset [9], etc.

### III. NEURAL NETWORK

Instead of creating and testing new architectures of neural networks for hand detection the architecture of YOLOv2 (You Only Look Once v2) was selected [10]. YOLOv2 is a fully convolutional neural network created out of 23 convolutional layers, 5 pooling layers, 2 routing layers, a reorganization layer and a single detection layer (see Fig. 2). The relatively low depth of the network makes it work very well in real time processing.

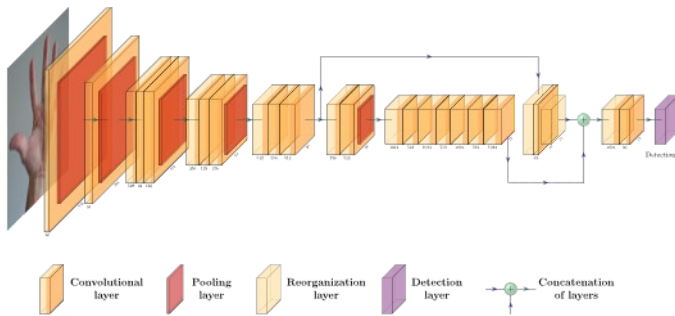


Fig. 2. YOLOv2 network architecture.

The actual network architecture is defined in configuration and weights files. The configuration file had to be adjusted to look for only one class, which meant changing the number of classes in the detection layer and changing the filter count in the preceding convolutional layer to the appropriate amount for the number of classes in the detection layer. In our testing, we selected 30 filters. To train the network for hand detection, the Python interpreter of the Darknet framework for PyTorch was used [11]. The neural network was trained for 150 epochs, where one epoch means a single pass through all the training data.

### IV. FINGER DETECTION AND GESTURE RECOGNITION

For finger detection a pretrained neural network trained for detection of hand key points was used. This neural network is part of the project OpenPose [12] to detect key points of specific parts of the human body. Out of the four networks, used convolutional pose machine is focused on hand key points detection. This network takes as an input a single image, in which is supposed to be a single hand. From this image the network on the output generates 22 heatmaps. Each of the first 21 heatmaps represent an approximate position of a single key point in the image and the last heatmap represents the background. From these heatmaps can be easily found the location of maximum, which represents the location of the found key point (see Fig. 3).

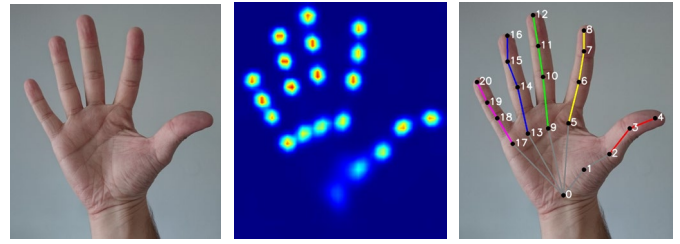


Fig. 3. Input image, combined heatmap and numbered hand key points.

One of the biggest downsides of OpenPose is the fact that it is trained to only detect key points of right hands. That means that the results of detection for the left hand are much worse than when using detection for the right hand. This issue can be avoided if the hand is known to be left, by flipping the image horizontally to effectively run the model over the right hand, followed up by flipping the detected key points around again to fit the left hand.

#### A. Left Hand Detection

To avoid the issues with left hands, the processing preceding the neural network was completely rewritten. The input image is flipped horizontally and stacked to the original. This combined image is passed through the network. The generated heatmap will have more higher peak values in the part of the image with the right or flipped left hand (see Fig. 4). From this is then easily decided which hand is in the input image and appropriate set of detected key points is selected for further processing.



Fig. 4. Left hand detection based on higher probabilities in each heatmap

#### B. Finger State Classification

From the detected key points, it is possible to get all the information needed for classifying gestures. As the key points are in a list of vertical and horizontal coordinates the distances between key points can be used to determine the pose of each finger and the angle of the line given by these points and the horizontal axis indicates the direction the hand or finger is pointed to.

From the detected key points, it is possible to get all the information needed for classifying gestures. As the key points are in a list of vertical and horizontal coordinates the distances between key points can be used to determine the pose of each finger and the angle of the line given by these points and the horizontal axis indicates the direction the hand or finger is pointed to.

##### 1) Finger Bends

The first thing needed for gesture classification is the state of bend for each finger. For all fingers except for thumb, which does not have a state of full bend, the bend state is defined in the gesture definition file by one of three states: *straight*, *partly\_bent*, *fully\_bent*.

### 2) Finger Spread

Another important parameter needed for gesture recognition signifies how far the fingertips are spread from each other. This parameter is just like finger bend state calculated using the distance between two points and is always defined for two neighboring fingers. In the gesture definition file, the spread of fingers is defined with one out of two possible states: *far*, *close*.

### 3) Thumb Position

The thumb in general can be in three different poses against the palm, these poses are in gesture definition named as: *over*, *close*, *far*.

### 4) Thumb Tip Position

Some hand gestures depend on the distance between the tip of the thumb and tip of other fingers. It may be very important to determine whether the fingertips are very close to each other and even touching. This is defined by the list of fingers the thumb is touching.

### 5) Thumb Direction

In some cases, the gesture may also need the direction of the thumb. Just like all other states of fingers, this is defined in the gesture definition file with states: *up*, *down*, *left*, *right*. Unlike with previous finger states, the direction of the thumb is calculated as an angle between the line defined by two points and positive direction of horizontal axis.

### 6) Hand direction

The last parameter defines the direction the hand is pointing to. It is calculated very similarly to the thumb direction and uses the same group of five states for the definition of gesture: *up*, *down*, *left*, *right*.

All proposed gestures are defined in a JSON file. These files contain a readable and easily modifiable structure with the name of the gesture and the definition of poses the finger can be in for the one gesture. Therefore, the list of available gestures could be easily extended with a new description.

## V. EVALUATION AND TESTING

To ensure ease of use, a graphical user interface for the application was created (see Fig. 5). For this purpose, the open-source cross platform Python library Kivy [13] was used.

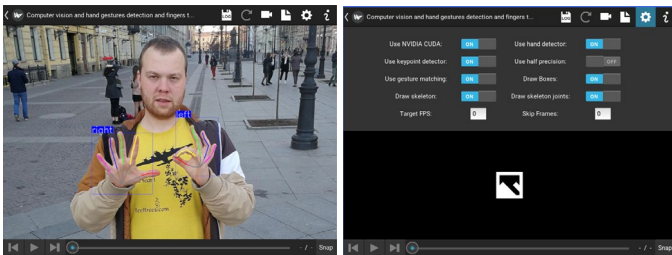


Fig. 5. Application UI and settings panel

The application's source code, including step by step installation guide for both Microsoft Windows and Linux based systems, is stored completely in a git repository [14].

As with any deep learning applications, it is highly recommended to use GPUs to speed up the forward pass of

input data through the neural network and out of the output. Parameters of all tested hardware are listed in Table I.

TABLE I. MAIN PARAMETERS OF USED GPUS AND CPUS

	NVIDIA GeForce		Intel Core	
	GTX 850M	GTX1060	i7 4700HQ	i5 8400
Cores	640	1280	4 (8 threads)	6 (6 threads)
Core Clock	0.901 GHz	1.607 GHz	2.4 GHz	2.8 GHz
Boost Clock	1.084 GHz	1.835 GHz	3.4 GHz	4.0 GHz
Memory	2 GB	6 GB	16 GB	8 GB
Technology	28 nm	16 nm	22 nm	14 nm
Architecture	Maxwell	Pascal	Haswell	Coffee Lake
Launch date	March 2014	July 2016	June 2013	October 2017

The neural network has a fixed input size, which means that all input frames are resized to the resolution set in the configuration file of the neural network before it was trained. In this case, the resolution is 416x416 pixels. As expected, the times needed for running the hand detector on any of the available CPUs provided unexceptional results as low as 0.61 frames per second using a mobile processor, the desktop CPU even though four generations newer and with higher clock speed, managed to be only three times as quick. Using the GPUs provided much better results, even the older mobile graphics card easily outperformed both tested CPUs by a big margin and managed to get to more than three times higher framerate than the desktop CPU. Although the mobile GPU did beat both CPUs by a big difference, using a newer desktop GPU provided a massive performance increase, although not as high as it could be, due to the bottlenecking of the graphics card by the CPU in the system. All the measured frame rates and times needed to process a single frame of a video sequence are listed in Table II.

TABLE II. DETECTION SPEED COMPARISON BETWEEN GPU AND CPU

	frames / second	time / frame [ms]
Intel Core i7 4700HQ	0.61	1,639.34
Intel Core i5 8400	1.83	546.45
NVIDIA GeForce GTX 850M	6.81	146.84
NVIDIA GeForce GTX 1060 6GB	28.91	34.59

The first test was to define if the hand is left or right. For the evaluation, 147 hands were used in a set of 101 testing images that contain people showing hands with different gestures using either one or both of their hands. This set of images was also taken with varying lighting conditions and in different environments. The implementation of the hand classifier managed to correctly classify the hand in 94.5% of all tested cases.

For the purpose of testing the gesture recognition system, eight gestures were predefined. These gestures were also

included in the creation of the dataset for evaluating the hand and gesture classifier and can be seen in Fig. 6.



Fig. 6. Predefined gestures: a) One, b) Two, c) Three, d) Four, e) Five, f) OK, g) Thumbs up, h) Thumbs down.

To evaluate, the same set of 101 images used to evaluate the classification of the left or right hand was used. These images were manually labeled with the gestures shown in them. The success rate was then calculated as a simple ratio between the correct classifications and total hand gestures used for testing. This produced a success rate of 79.8%.

The evaluation dataset contains 119 hands, on which the hand key point detector subjectively predicts the locations of key points correctly. Out of these 119 hands, each of the tested gestures was represented with approximately 10 to 18 occurrences in the dataset. On top of the tested gestures, 16 hand poses that did not match any of the predefined gestures were included to also test if the gesture matching logic understands the unknown hand poses correctly. From the results, a confusion matrix in Fig. 7 was also created for visual representation of the accuracy. As is visible, most of the classifications are on the main diagonal, which means these classifications were correct, and if they were not, in most cases the gesture was classified as an unknown gesture.

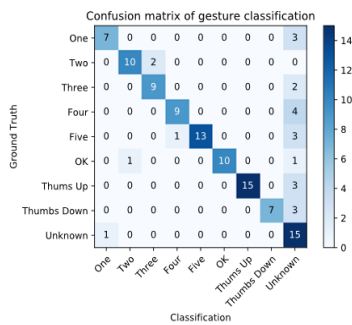


Fig. 7. Confusion matrix for predicted gestures

## VI. CONCLUSION

The goal of the research was to study and analyze possible approaches to hand detection, gesture recognition and finger tracking, select one of the possible approaches to the issue and to create a multiplatform application capable of processing images, video sequences and a camera stream.

Because neural networks need a lot of training data to produce usable results, the training dataset was created with a combination of the EgoHands dataset, MPII Human Pose estimation dataset and a couple of videos from the New Zealand Sign Language dictionary. The combined dataset provided a high variety of hands in different environments, lighting and poses, and contained over 6000 images, usually with more than one hand in each. After training, the neural network YOLOv2 resulted in very good detection results with 89.2% of all relevant objects, in this case hands, detected. Out

of all the detections, the network managed to find the hands properly in 85.7% of all cases.

Even though the network is from the project OpenPose, the processing of the image before and after the forward pass through the neural network is completely different from the OpenPose implementation. The additional processing adds the capability to recognize whether the hand sent through the network was left or right correctly in almost 95% of all cases, which adds the possibility to implement gesture recognition with gestures specific for either left or right hand.

The whole detection logic was connected to a graphical user interface, that makes the interaction with the logic easy and user friendly while providing additional functionality compared to using just the script included in the module with hand tracking class.

## REFERENCES

- [1] Gesture Recognition using OpenCV + Python, <http://vipulsharma20.blogspot.com/2015/03/gesture-recognition-using-opencv-python.html>. Last accessed 10 August 2019
- [2] Extending the hand tracker with snakes and optimizations, <http://www.morethantechical.com/2013/05/26/extending-the-hand-tracker-with-snakes-and-optimizations-w-code-opencv/>. Last accessed 10 August 2019
- [3] Du, H., Charbon, E.: 3D Hand Model Fitting for Virtual Keyboard System. In: 2007 IEEE Workshop on Applications of Computer Vision (WACV '07). IEEE, USA (2007). <https://doi.org/10.1109/WACV.2007.3>
- [4] Hand gesture recognition via model fitting in energy minimization, <http://www.morethantechical.com/2010/12/28/hand-gesture-recognition-via-model-fitting-in-energy-minimization-w-opencv/>. Last accessed 11 August 2019
- [5] Vinh, T.Q., Tri, N.T.: Hand gesture recognition based on depth image using kinect sensor. In: 2nd National Foundation for Science and Technology Development Conference on Information and Computer Science (NICS), pp. 34--39. IEEE, Vietnam (2015). <https://doi.org/10.1109/NICS.2015.7302218>
- [6] Mittal, A., Zisserman, A., Torr, P.H.S.: Hand detection using multiple proposals. In: Proceedings of the British Machine Vision Conference (BMVC). United Kingdom (2011)
- [7] Bambach, S., Lee, S., Crandall, D.J., Yu, C.: Lending A Hand: Detecting Hands and Recognizing Activities in Complex Egocentric Interactions. In: IEEE International Conference on Computer Vision (ICCV), pp. 1949--1957. IEEE, Chile (2015). <https://doi.org/10.1109/ICCV.2015.226>
- [8] New Zealand Sign Language Dictionary, <https://www.nzsl.nz>. Last accessed 11 August 2019
- [9] Andriluka, M., Pishchulin, L., Gehler, P., Schiele, B.: 2D Human Pose Estimation: New Benchmark and State of the Art Analysis. In: IEEE Conference on Computer Vision and Pattern Recognition, pp. 3686-3693. IEEE, USA (2014). <https://doi.org/10.1109/CVPR.2014.471>
- [10] YOLO: Real-Time Object Detection, <https://pjreddie.com/darknet/yolov2/>. Last accessed 12 August 2019
- [11] Yet Another Implimentation of Pytroch 0.4.1 and YoloV3 on python3, <https://github.com/andy-yun/pytorch-0.4-yolov3>. Last accessed 12 August 2019
- [12] OpenPose: Real-time multi-person keypoint detection library for body, face, hands, and foot estimation, <https://github.com/CMU-Perceptual-Computing-Lab/openpose>. Last accessed 12 August 2019
- [13] Kivy: Cross-Platform Python Framework for NUI Development, <https://kivy.org/#home>. Last accessed 12 August 2019
- [14] Computer vision and hand gestures detection and fingers tracking, <https://gitlab.com/travenec/computer-vision-and-hand-gestures-detection-and-fingers-tracking>. Last accessed 12 August 2019

# Design of lens antennas for E-band communication

Petr Kadera

Department of Radio Electronics  
Brno University of Technology  
Brno, Czech Republic  
xkader05@vutbr.cz

**Abstract**—The paper presents performance comparison of lens horn antennas for millimeter wave backhaul system. The perforated flat dielectric lens horn antenna based on transmit-array and integrated lens antenna are compared, respectively. The frequency ranges of 71/76 GHz and 81/86 GHz (E-band) which are perspective for the point-to-point 5G communications are fully covered. The realized gain of proposed antennas exceeds 38 dBi and side-lobe suppression is above 14 dB.

**Keywords**—horn antenna, transmit-array, perforated lens, integrated lens, E-band, point-to-point, 5G, communication..

## I. INTRODUCTION

In the present time, the mobile operators and internet service providers must provide a backhaul systems with throughput of 1-10 Gb/s. To fulfill this requirement, the point-to-point radio links usable in unlicensed frequency bands can be used. One of the suitable frequency band is E-band with frequency ranges between 71 GHz and 76 GHz and 81 GHz and 86 GHz, which are also planned for 5G communications [1]. The European regulation (ETSI) prescribes that the antennas for E-band frequency range have to comply the gain higher than 38 dBi (half-power beam width below  $2^\circ$ ) which means that those radio links can provide large distance communication, up to several kilometers [2]. Also the requirement of sufficient side-lobe suppression is necessary for the antenna interference minimization and meeting the ETSI radiation pattern envelope (RPE) compliancy with class at least 2 or 3. Low level of the first side-lobe has also practical utilization in facilitation of radio links pointing during mounting radios on the masts and roofs. For this application is optimal to use reflector or lens-based antennas.

In this paper, the comparison of two antennas for high speed communication in E-band millimeter wave frequency band is presented. The perforated lens horn antenna based on transmit-array and the elliptical integrated lens antenna are designed and their performance is then evaluated. The numerical simulations were performed by using CST Microwave Studio. The conclusions with suggested improvements of the structures are further proposed.

## II. ANTENNAS DESIGN

### A. Perforated flat lens horn antenna (transmit-array)

The design of perforated flat lens is based on the Fermat's principle of equality of electrical path lengths [3] when the required phase correction of each unit cell of the lens aperture

is calculated as shown in Fig. 1, where  $\lambda_0$  is the free space wavelength at the desired frequency,  $F$  is the focus distance from the phase center point of the feed source to the center of the lens,  $r$  is the distance from the central element to the side elements of the lens. The term  $\pm 2\pi N$  is added to the calculation in order to keep the required phase value within the range of  $0-360^\circ$ .

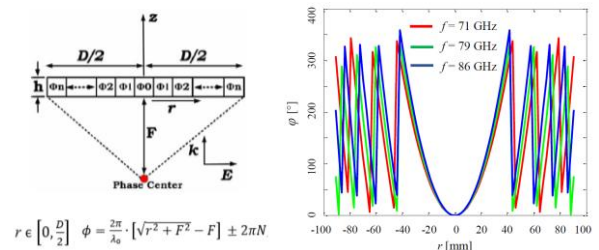


Fig. 1. Calculated required phase correction of unit cells.

The perforated dielectric structure composed of unit cells with various hole diameters in the range between 0.4 mm to 1 mm for phase correction was chosen taking into account the ease of manufacture by drilling (subtractive manufacturing) or by 3D printing (additive manufacturing). The unit cell is also customized to the waterproof structure requirement for operation in the outdoor. For obtaining the unit-cell phase response, the numerical method of TEM-waveguide model with properly set perfect electric conductor (PEC) and perfect magnetic conductor (PMC) boundary conditions was used (Fig. 2.). The dielectric material used for lens design was chosen to be Teflon with relative permittivity  $\epsilon_r$  of 2.06 and tangent loss  $\text{tg}\delta$  of 0.0002 at 86 GHz [4]. The dimensions of the unit cell are about  $0.6 \lambda_0$ , the diameter of the lens  $D$  is 180 mm, the length of the horn  $L$  is 234 mm and the thickness of the lens  $t$  is 22 mm (including 5 mm covering layer) which corresponds to the length to diameter ratio  $L/D$  of 1.3 (Fig. 3).

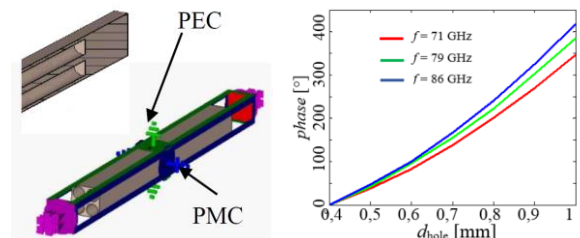


Fig. 2. Numerical model and unit cell phase response.

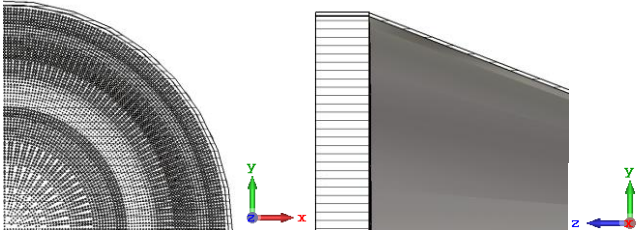


Fig. 3. Fraction of the perforated lens (white-substrate, black-perforation) and horn antenna.

The phase on the antenna aperture for the central frequency of 78.5 GHz is plotted in Fig. 4. The simulated realized gain ( $G_r$ ), side-lobe suppression in E and H planes ( $SLS_E$ ,  $SLS_H$ ), the input reflection coefficient ( $S_{11}$ ) and ETSI radiation pattern envelope are shown in Figs. 5-7.

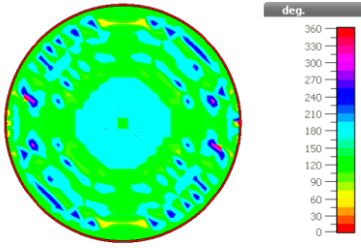


Fig. 4. The phase on the perforated lens antenna aperture,  $f = 78.5$  GHz.

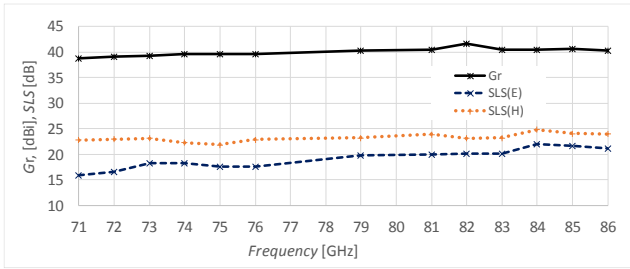


Fig. 5. Simulated parameters of perforated lens horn antenna.

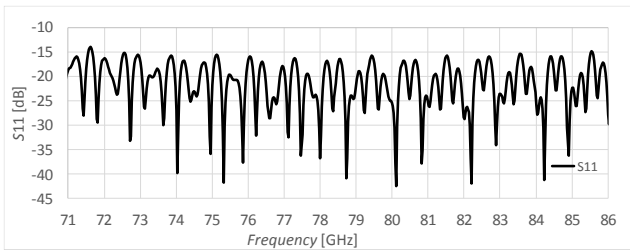


Fig. 6. The input reflection coefficient of perforated lens horn antenna.

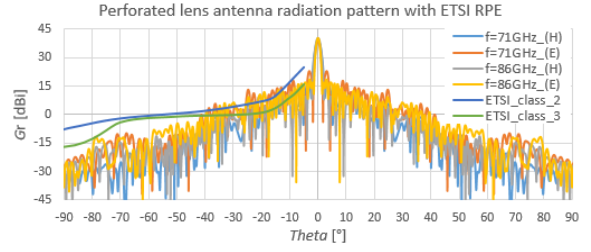


Fig. 7. ETSI radiation pattern envelope of perforated lens horn antenna.

It can be observed that the phase response of the unit-cell for the same hole diameter varies with the frequency what makes the design more complicated. The phase on the antenna aperture is therefore not constant for all the frequencies. The simulated gain of the antenna is between 38.3 dBi and 40.3 dBi for the frequency range of 71 GHz and 86 GHz, respectively. The side-lobe suppression in E and H planes varies from 16 dB to 22 dB and from 23 dB to 24 dB, respectively. The input reflection coefficient is lower than -14 dB and the antenna efficiency is around 87 %. The antenna radiation patterns exceed ETSI RPE in class 2 and 3 and therefore it needs better optimization of the lens phasing structure.

### B. Integrated lens antenna

The integrated lens antenna can also be used for E-band communications plus it has a good capability of beam-steering, which makes it a good candidate for using in flexible-beam 5G communication systems [5][6]. In dependence of beam-steering angle requirements, the shape of the lens can differ. The elliptical lens is better for beam-steering in the range of 15-25°, however, the semi-sphere lens is better for beam-steering angle larger than 25° [7].

The lens design equations are as follows:

$$\left(\frac{x}{a}\right)^2 + \left(\frac{y}{b}\right)^2 = 1 \quad (1)$$

$$L = e \cdot a \quad (2)$$

$$e = \sqrt{1 - \left(\frac{b}{a}\right)^2} \quad (3)$$

where  $x$  and  $y$  represent coordinates of ellipse axes,  $a$  is main half-axle and  $b$  is secondary half-axle,  $L$  determines the length of lens extension and  $e$  is the lens eccentricity. The integrated lens antenna structure with focal point  $f$  and its model is shown in Fig. 8. The material used for lens design was Teflon.

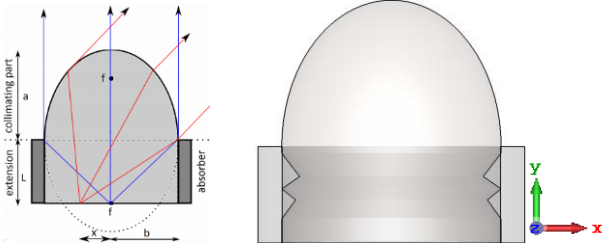


Fig. 8. Integrated lens antenna with its parameters and simulation model.

The diameter of the lens is 180 mm, the length of main half-axle is 119.2 mm and the length of extension is 78.1 mm what makes antenna to be 197.3 mm high. The eccentricity of ellipse is then 0.95. The antenna is excited in the focal point by open rectangular waveguide WR-12 with directivity of 8.2 dBi.

The phase on the antenna aperture (beyond the lens) for the central frequency of 78.5 GHz is plotted in Fig. 9. The simulated realized gain ( $G_r$ ), side-lobe suppression in E and H planes ( $SLS_E$ ,  $SLS_H$ ), the input reflection coefficient ( $S_{11}$ ) and ETSI radiation pattern envelope are shown in Figs. 10-12.

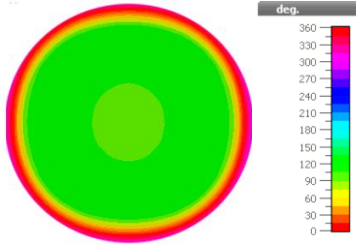


Fig. 9. The phase on the integrated lens antenna aperture,  $f = 78.5$  GHz.

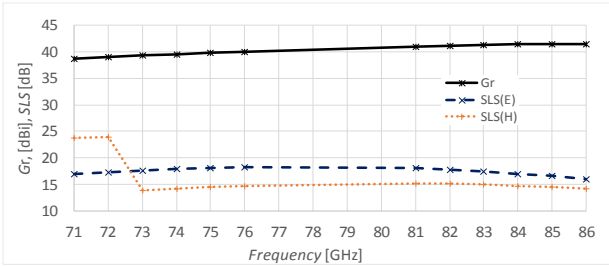


Fig. 10. Simulated parameters of integrated lens horn antenna.

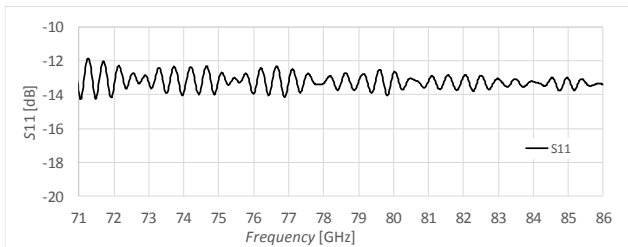


Fig. 11. The input reflection coefficient of integrated lens horn antenna.

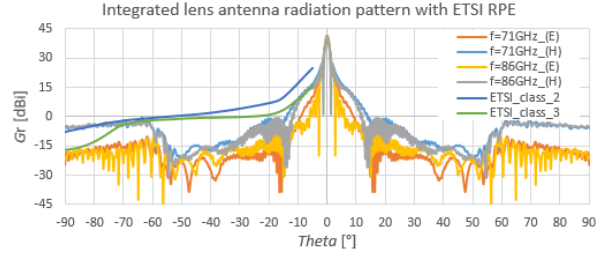


Fig. 12. ETSI radiation pattern envelope of integrated lens horn antenna.

It can be observed that the phase on the antenna aperture is almost constant. The simulated gain of the antenna is between 38.7 dBi and 41.5 dBi for the frequency range of 71 GHz and 86 GHz, respectively. The side-lobe suppression in E and H planes varies from 16 dB to 18 dB and from 14 dB to 24 dB, respectively. The input reflection coefficient is lower than -12 dB and the antenna efficiency is around 76 %. The antenna radiation patterns in E and H planes comply with ETSI RPE in class 3 up to 90° and 61°, respectively. Further optimization of the lens structure could improve those parameters.

### C. Antennas comparison

The main advantages of the perforated lens antenna are light and thin lens of thickness only 22 mm, which could be further reduced to 18 mm, and the possibility to use short antenna core due to phasing elements. The main disadvantages of this antenna are the larger possibility of the lens detuning caused by the inaccuracy of manufacturing process and the difficulty to design large lens structure of diameter 180 mm, which is also connected with the exceeding of ETSI radiation pattern envelope.

The main advantages of the integrated lens antenna are relatively easy design procedure and the possibility to be used only with feeding network without need of a metal core. The main disadvantage of this antenna is higher weight in compare to perforated lens antenna caused by bulky lens.

The beam-steering capabilities of this antennas could be also realized, e.g. by switching network with slotted waveguide focal array as is presented in [5] and [8].

## III. CONCLUSIONS

In this paper, the design of perforated lens and integrated lens antennas is presented. Both structures are compared in terms of realized gain, side-lobe suppression in E and H planes, impedance matching and the compliance with ETSI radiation pattern envelope. Pros and cons of proposed antennas are then evaluated. The 5G communication requirements of the sufficient antenna gain and side-lobe suppression are successfully fulfilled. The requirement of beam-steering capabilities could be satisfied by using appropriate switching network and the antennas performance in terms of ETSI radiation pattern envelopes could be further improved by optimization of the lens structures. The proposed antennas may then be suitable for flexible beam 5G communication systems.

## ACKNOWLEDGMENT

The research described in this paper was financed by the Czech Ministry of Education in the frame of the National Sustainability Program under grant LO1401. For the research, the infrastructure of the SIX Center was used. Thanks to Racom, s. r. o. for directing the assignment on the basis of which the research was carried out. Further thanks to Tomas Mikulasek for valuable discussion and helpful comments.

## REFERENCES

- [1] A. V. Raisanen, J. Zheng, J. Ala-Laurinaho, S. Karki and V. Viikari, "Millimeter-Wave Antennas for 5G," in: *2018 11th Global Symposium on Millimeter Waves (GSMM)*, Boulder, CO, USA, 2018, pp. 1-4.
- [2] Standard ETSI EN 302 217-4. Fixed Radio Systems; Characteristics and requirements for point-to-point equipment and antennas; Part 4: Antennas. France. 2016.
- [3] M. K. T. Al-Nuaimi and W. Hong, "Compact size pyramidal horn lens antenna for E-band gigabit point-to-point communications," in: *Proceedings of 2014 3rd Asia-Pacific Conference on Antennas and Propagation*, Harbin, 2014, pp. 1183-1186.
- [4] C. A. Balanis, "NASA Technical Note: Measurement of dielectric constants and loss tangents at E-band using a Fabry-Perot interferometer. Langley Research Center, Dec. 1969. Available from: <https://ntrs.nasa.gov/archive/nasa/casi.ntrs.nasa.gov/19700003017.pdf>.
- [5] A. Artemenko, A. Mozharovskiy, A. Sevastyanov, V. Ssorin and R. Maslennikov, "Electronically beam steerable lens antenna for 71–76/81–86 GHz backhaul applications," in: *2015 IEEE MTT-S International Microwave Symposium*, Phoenix, AZ, 2015, pp. 1-4.
- [6] S. K. Karki, J. Ala-Laurinaho, V. Viikari and R. Valkonen, "Lens antenna design for E-band point-to-point radio links," in: *2017 Progress In Electromagnetics Research Symposium - Spring (PIERS)*, St. Petersburg, 2017, pp. 1625-1631.
- [7] A. Karttunen, J. Ala-Laurinaho, R. Sauleau, and A. V. Raisanen, "Reduction of Internal Reflections in Integrated Lens Antennas for Beam-Steering," in: *Progress In Electromagnetics Research*, Vol. 134, 63-78, 2013.
- [8] L. Dussopt, A. Mognache, T. Potelon and R. Sauleau, "Switched-beam E-band transmitarray antenna for point-to-point communications," in: *2017 11th European Conference on Antennas and Propagation (EUCAP)*, Paris, 2017, pp. 3119-3122.

## System for analysis of FSO terminal vibrations

Marek Novák, Petr Skryja

### Abstract

This poster presents a system whose task is to gather vibrational data from Free Space Optical (FSO) communication terminal. As shown in [1, 2] the atmosphere and specifically the wind influences the FSO link performance. The purpose of gathered data is to analyze the response of the mechanical fixture to wind blasts. Based on this known response, a mathematical model will be created allowing to make a short-time prediction of FSO terminal deviation, which will be used in the Acquisition, Tracking and Pointing (APT) algorithm described in [5] applied in the context of FSO.

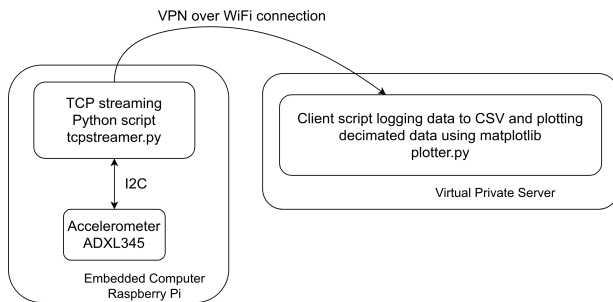
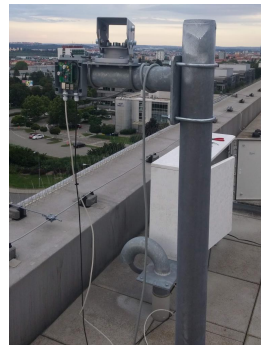


Fig. 1: Block diagram of logging vibration system



Fig. 2: Prototype of device for vibration measurement



FSO link developed at BUT is fully photonic - incoming optical beam is focused using a Fast Steering Mirror (FSM) into an optical fibre. The fibre core diameter is in the order of tens of micrometers, therefore any vibration source or atmospheric turbulence deviates the beam and causes a signal loss. The analysis of present vibrations helps to improve the APT algorithm and to reduce the impact of these effects. As herein shown device measures uniquely the effects of vibrations, the obtained data can be also used to separate and compare effects of vibrations and atmospheric turbulence to the FSO link quality.

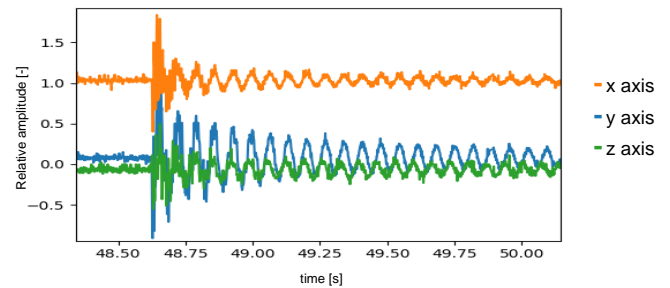


Fig. 3: Oscillation of artificial created vibration in time domain

Fig. 1 shows the block of the system present in Fig. 2. The resulting vibration data are then shown in time domain in Fig. 3 and the frequency analysis (spectrum in Fig. 4) helped to measure the resonant frequency of the vibrating fixture from Fig. 2. According to Fig. 3 it is 14.6 Hz. From the time domain graph, it can be seen that there is a dumping effect in the signal, which if known, along with the resonant frequency, allows to predict the movement of the whole fixture after an air gust.

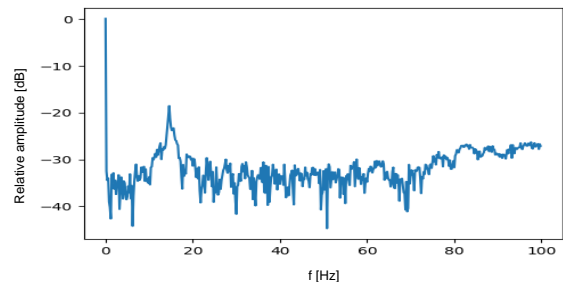


Fig. 4: Oscillation of artificial created vibration in frequency domain

- [1] BARČÍK, P.; WILFERT, O.; DOBESCH, A.; KOLKA, Z.; HUDCOVÁ, L.; NOVÁK, M.; LEITGEB, E. Experimental measurement of the atmospheric turbulence effects and their influence on performance of fully photonic wireless communication receiver. *Physical Communication*, 2018, vol. 31, no. 1, p. 212-217. ISSN: 1874-4907.
- [2] V. Brazda, O. Fiser, Z. Chladova, J. Poliak and V. Schejbal, "On wind influence on FSO link attenuation," *2013 7th European Conference on Antennas and Propagation (EuCAP)*, Gothenburg, 2013, pp. 966-968.
- [3] M. Matsumoto, K. Osawa, S. Hotta and K. Wakamori, "Innovative tracking system for next generation FSO systems under massive earthquakes," *2015 International Conference on Optical Network Design and Modeling (ONDM)*, Pisa, 2015, pp. 233-238. doi: 10.1109/ONDM.2015.7127304
- [4] T. Mitsev and E. Ferdinandov, "Methodology for realization of given BER in FSO systems under effect of internal and external noises," *2015 Conference on Microwave Techniques (COMITE)*, Pardubice, 2015, pp. 1-4. doi: 10.1109/COMITE.2015.7120319
- [5] NOVÁK, M.; DOBESCH, A.; WILFERT, O.; JANÍK, L. Visible Light Communication transmitter position detection for use in ITS. *OPT SWITCH NETW*, 2018, no. 2, p. 1-8. ISSN: 1573-4277.

# Hardware cryptographic module for FPGA with dynamic hash functions routing

Michal Kerndl

Electrical Engineering and Communication  
Brno University of Technology  
Brno, Czech Republic  
xkerndl00@vutbr.cz

Pavel Šteffan

Electrical Engineering and Communication  
Brno University of Technology  
Brno, Czech Republic  
steffan@feec.vutbr.cz

**Abstract**—This paper deals with design of hardware cryptographic module for System-on-Chip that can be simulated on FPGA. The main function of this module is dynamic routing of SHA-3 hash function candidates that are commonly used s X11 hash algorithm. Proposed design was verified and evaluated using Virtual Platform methodology and aims to be an example of development of system based on Virtual Platform. Designed architecture can be deployed on FPGA or real hardware platform. This hardware can be used in Internet-of-Things or another related applications.

**Keywords**—dynamic routing; hash function; system-on-chip; virtual platform;FPGA; internet-of-things

## I. INTRODUCTION

In recent years, the System-on-Chip (SoC) becomes key building block for Internet-of-Things (IoT) due to complexity and hardware requirements that still increasing. SoC can integrate a variety of system functions, for example a video and image processing, connectivity etc. Usually these system functions are implemented using a mix of software and hardware [1].

The most important building block in SoC is processor, that can provide flexibility and upgradeability [1]. In other hand, there are cryptographic functions, that are commonly used in security connections, verifying etc. that uses a lot of processor resources.

This article deals with hardware implementation of selected hash functions, that can be implemented on low-level register-transfer design (RTL) that significantly increase speed and efficiency of their computing. We propose dynamic routing of these hash functions that can lead to more specific output value. In this work is described an example of how to achieve a specific order of hash functions. Proposed design was modeled by Virtual platform method, that requires to build and connect design block, typically written in VHDL programming language.

## II. SYSTEM ON CHIP

### A. Virtual Platform

Used design method requires to create each component first as a model. These components needs to be interconnected

by bus or connections. Verification of design can be done in design software and next step is deploying the Virtual Platform on a host hardware to confirm its function [2]. SoC Virtual Platform is great cost reduction and quality improvement due to time to market requirements.

As proposed in article [3] the comparison of running such software on a real hardware and SoC Virtual Platform shows similar results. The flexible development is possible without actual hardware and complete design can be used on target hardware immediately. Similar design was proposed in article [4] and [5], this work is based on its proposal.

Proposed design can be seen on Fig. 1 that shows the block diagram of SoC with main CPU ARM core that is connected to flash and DDR memory and connection modules such as Wi-Fi, Bluetooth, Ethernet, USB etc. Hardware cryptographic module contains X11 hash functions as well as SHA-256, RSA and AES functions.

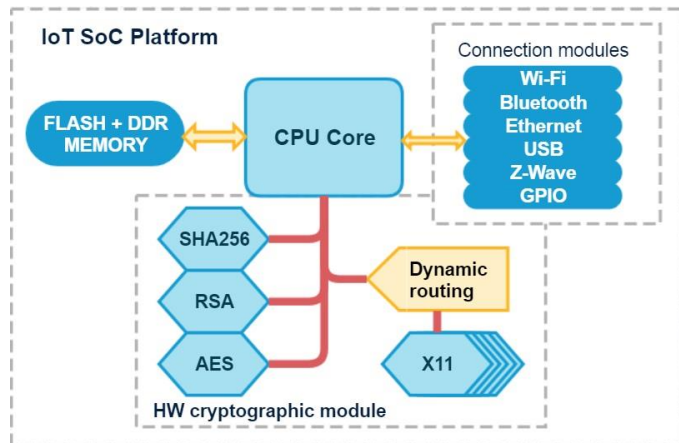


Fig. 1. Block diagram of proposed SoC Virtual Platform design

## III. HARDWARE CRYPTOGRAPHIC MODULE

Main idea of this article is Hardware cryptographic module that can be seen on Fig. 1. Hash functions are passed through Dynamic Routing module. Input and output can be selected and hash functions can be routed to each other to get more advanced output. It means that the X11 algorithm (that is made by 11 different hash algorithms) can be re-routed and

inputs or outputs of partial functions can be used to get new, more specific output value. Output depends not only on the hash functions, but also on their selected order. Internal structure of dynamically routed multi-hash algorithm is shown on Fig. 2.

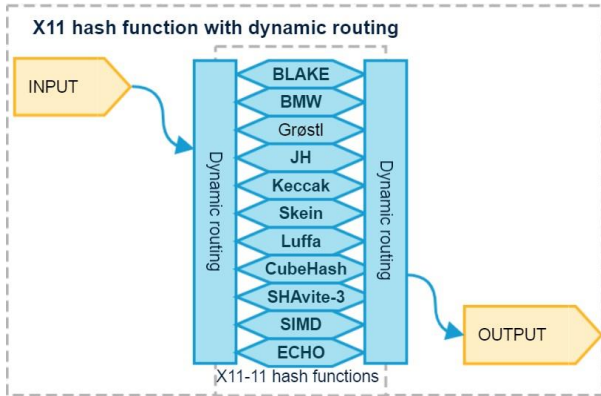


Fig. 2. Dynamic routing of multi-hash function

### A. Used cryptographic functions

Due to the often usage in wide variety of applications, the SHA-256, RSA and AES was implemented. Dynamically routed hash algorithms was chosen as SHA-3 candidates, because they are considered to be very secure and fast hash functions. Selected algorithms JH, Keccak and Skein was implemented in VHDL and verified individually by their test-bench to proof working principle of dynamic routing.

### B. Dynamic routing

The main idea of proposal is Dynamic Routing inside the cryptographic module. This was solved by usage of Multiplexer and Demultiplexer (13 to 1). Connecting inputs/outputs marked as "X" ports (Fig. 3) ensures that each hash function is routed to another. Binary combination on "Sel" pins corresponds to multiplexing output pins ("A"-"M") and their selection is causing the routing of hash functions in selected order.

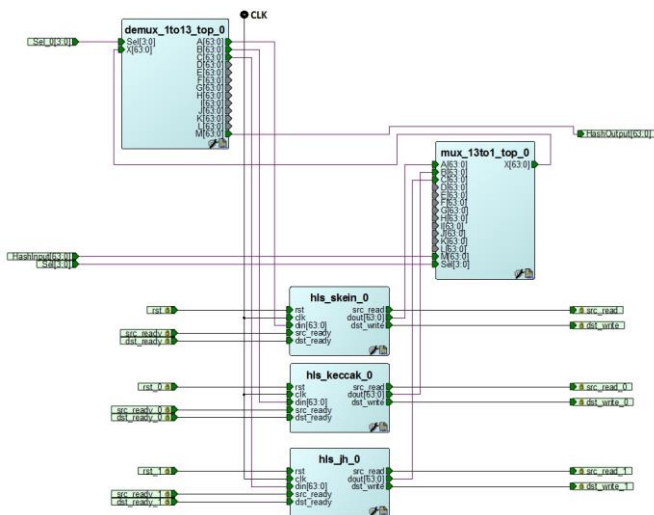


Fig. 3. Structure inside Dynamic routing block (three example functions)

All components are driven by master clock signal "CLK". Hash input ("M") must be selected on start-up routine, and routed to first hash function block. These are also driven by "CLK" and needs reset signal on "RST" pin on start-up.

The selected block will start hashing for data on "din" when all "handshake" signals are correct (ready of source "src\_ready" and "dst\_ready") by rising edge on "src\_read". When the hash computation is completed, output data are sent to "dout" by rising edge on "dst\_write" pin. For better managing of middle state errors, it is possible to add RAM memory blocks in between the Multiplexer and Demultiplexer as a cache. Unconnected pins ("D" - "L") will be used for the rest of X11 hash functions.

## IV. SIMULATION AND TEST-BENCH RESULTS

For design and modeling of VHDL components was used Libero SoC v11.9 software. Example was reduced to three different hash functions Skein, Keccak and JH due to high logic resources usage of all X11 hash functions. Full implementation will require high end FPGA such as Xilinx Virtex family or Altera Stratix.

Reduced example design was compiled and takes 32.000 4LUT (look-up tables) and 14.000 DFF (D flip-flop). This resources can be provided by available "Smart Fusion 2 SoC FPGA" development board. Detailed usage of logic resources can be seen on Fig. 4.

### Detailed Logic Resource Usage

Type	4LUT	DFF	Percentage
Fabric Logic	138128	26155	94.68
RAM64x18 Interface Logic	216	216	18.05
RAM1K18 Interface Logic	0	0	
MACC Interface Logic	0	0	
Total Used	138344	26371	

Fig. 4. Detailed logic resource usage (three example functions)

This development board is ideal for general purpose functions and contains a lot of resources in low density such as ARM Cortex-M3 processor, comprehensive microcontroller subsystem and a lot more features. The power is low as 7 mW in stand-by mode.

This board is also supported in Libero SoC and was used for simulation and test-bench of proposed design. The example of dynamic routing is shown on Fig. 5.

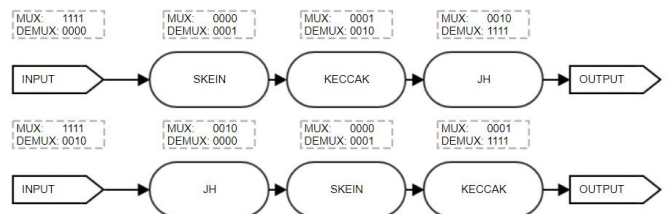


Fig. 5. Structure inside Dynamic routing block (three example functions)

## ACKNOWLEDGMENT

The work was supported by the Brno University of Technology project no. FEKT-S-14-2300: "New types of electronic circuits and sensors for specific applications".

## V. CONCLUSION

In this paper we proposed Dynamic routing solved by basic components, such as Multiplexer and Demultiplexer. This routing was used to dynamically connect inputs/outputs of particular SHA-3 candidate hash functions to achieve more specific hash output. So the original information can be hashed or verified in more complex way.

For successful usage of dynamically routed hash functions, the end user needs to know what functions was used, and what was exact order of processing. This means that the security of hashed message is improved, and system is more complex and durable.

In other words, the SoC can calculate hash output for given input, based on order of particular functions. This can increase security, because the hashed information needs to be provided (or can be kept in secret) with exact order of used functions, to be verifiable by other users. This system can also be used in many scenarios, such as building decentralized distributed database also known as "Blockchain" etc.

## REFERENCES

- [1] TANURHAN, Yankin and Pieter VAN DER WOLF. 2013. Processors as SoC building blocks. *2013 IFIP/IEEE 21st International Conference on Very Large Scale Integration (VLSI-SoC)*. IEEE, , 286-287.
- [2] EL-MOURS, Magdy A., Ayman SHEIRAH, Mona SAFAR and Ashraf SALEM. 2014. Efficient embedded SoC hardware/software codesign using virtual platform. *2014 9th International Design and Test Symposium (IDT)*. IEEE, 2014(9), 36-38.
- [3] LEE, Hyoung-Ro, Chi-Ho LIN, Ki-Hyuk PARK, Won-Jong KIM and Han-Jin CHO. 2017. Development of SoC virtual platform for IoT terminals based on OneM2M. *2017 International SoC Design Conference (ISOC)*. IEEE, 2017(5), 320-321.
- [4] VARGHESE, Nelson Vithayathil, Won Jong KIM, Shin Seok KANG and Hyo Seung LEE. 2018. Design and verification of secure IoT hub based on virtual SoC platform. *2018 International Conference on Electronics, Information, and Communication (ICEIC)*. IEEE, 2018(5), 1-3.
- [5] YOON, Sungjae, Kihyuk PARK, Wonjong KIM and Hanjin CHO. 2018. Power estimation of cryptographic modules using virtual SoC platform. *2018 International Conference on Electronics, Information, and Communication (ICEIC)*. IEEE, , 1-3.

# Wifi Access Point Detector

Erik Herceg  
Department of Radio electronic  
Brno University of Technology  
Brno, Czech Republic  
herceg@feec.vutbr.cz

**Abstract**—This article is focused on the detection of the position or more accurately, the course of the man, who controls the drone. This experiment was done with commercially available components to reduce costs or replace expensive radars for drone detection. The concept of the device consisted of using low-cost WiFi modules working in 2.4 GHz and also 5 GHz. These modules are providing information about all visible access points that can be seen in a close area. With this comes the main problem with overloaded ISM frequency band, where all of these devices work. The connection between individual modules is ensured with an ethernet switch, and the calculations and data are processed in the computer. Every module is connected to a directional antenna. The antenna's main lobe takes an angle of 36°, so ten antennas were used. This article brings a different view of drones problematic and its elimination in prohibited areas. This type of detection was not described, and there was no article where a similar method was used.

**Keywords**—Drones, WiFi, Acces Point, Safety.

## I. INTRODUCTION

With the expansion of drones and its availability and low cost, the danger connected with drones has increased. Places such as nuclear power plants, airports, and other essential buildings have to be protected, and they are threatened by drones. New types of drones have complicated systems and can fly in stand-alone mode for a while. With advanced modulations in new drones, jamming or taking over the drone is an impossible task. Thus, if communication between the controller and the drone can't be interrupted, or drone tracked, find a person with a mobile phone connected through the access point to the controller should be more comfortable. The majority of the controllers is connected to the mobile via WiFi. The distance between the controller and the mobile is short, so the signal strength between AP of mobile and controller is always set to the lowest possible level.

Many drone detection experiments have been published. This can be done in three primary ways: acoustically, optically, and in the frequency spectrum. The acoustic method works in principle of directional microphone, that checks the acoustic spectrum from 700 kHz to 16 kHz. This method is applicable in a few hundreds of meters. As in any method, this is only usable in open area, without any noises that can be caused by people and vehicles in public places.

The optical method is also inaccurate, because of the environment and mainly the sun and its brightness, which cause problems for cameras.

The last method is to scan the radio frequency band. Many commercial controllers are connected with the drone at 2.4 GHz, but drone does not act as an access point, and the communication is not standard. This method is mostly used but also has its problems. As this communication runs in the ISM band, this spectrum is also overload, and the detection of a drone could be problematic.

Many drone detection articles have been published, and many methods have been used. The optical method was presented in [1], where a PTZ camera was used for drone detection, and the detection accuracy and speed was compared for various detection models. The artificial intelligence for drone detection was presented in [2]; the accuracy achieved almost 92 %.

The frequency modulated continuous wave radar was used in [3]. The working frequency was 8.75 GHz. At this frequency and with the use of Doppler matrices, the drone could be detected up to two kilometers. The small area of drone and the plastic parts are challenging to detect. In the radar nomenclature, this fact is called radar cross-section. The micro-Doppler radar for drone detection was used in [4]. This article is focused on the comparison of drones, birds, and other flying objects. Frequency of used radar was 9.7 GHz, and four types of objects were supposed to be detected and specified. In article [5] two methods of drone detection were presented. The SDPR and MSDPR passive radars for drone detection were described and compared. MSDPR radar is able to capture the distance and complete path of the drone flight. This was compared with real GPS data, and the results were. All these types of radars were compared in [6]. The analog and digital FMCW radar were compared with Noise radar. The digital FMCW radar achieved results below a range of 50 m, which cannot be used in the real application. Analog FMCW radar had even worse results when the range was slightly more than 30 m, and with the Noise radar, the results were similar.

As mentioned above, drone detection is not so simple. Drone detection has many obstacles, like a small RCS drone, ground clutter is also a problem, and the difference between drone and bird is also tricky. This has brought an idea, that's researched in this article and focuses on the man who controls the drone instead of looking for the drone, which is complicated. It cannot be said that this task is simple, due to the low RF power of the AP controllers, but the probability of success is higher and also the cost of the detector should be lower.

## II. CONCEPT OF WIFI DETECTOR

The essential parts of the WiFi detector are shown in Fig. 1. As the input part, the directional antennas for 2.4 GHz and 5 GHz are used. The input connector of antennas is SMA connector. As the WiFi receiver has U.FL connector, a reduction board was used. The reduction board has two SMA connectors for connection with antenna and U.FL connectors for WiFi module. Between these connectors, there is a  $50\ \Omega$  trace and bandpass filter for unwanted frequencies filtration. The filter is made of lumped components. The WiFi receiver has its own MCU, which sends all essential parameters of measured access points via Ethernet to PC. All 10 modules send continuously information about all visible APs every second. Required parameters are RSSI, SSID, and channel and its frequency.

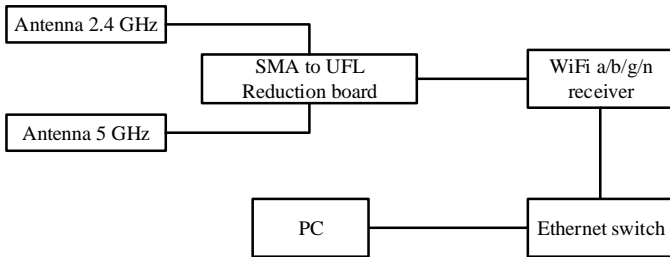


Fig. 1. Basic block scheme of the module used in the Access Point detector.

### A. Antennas

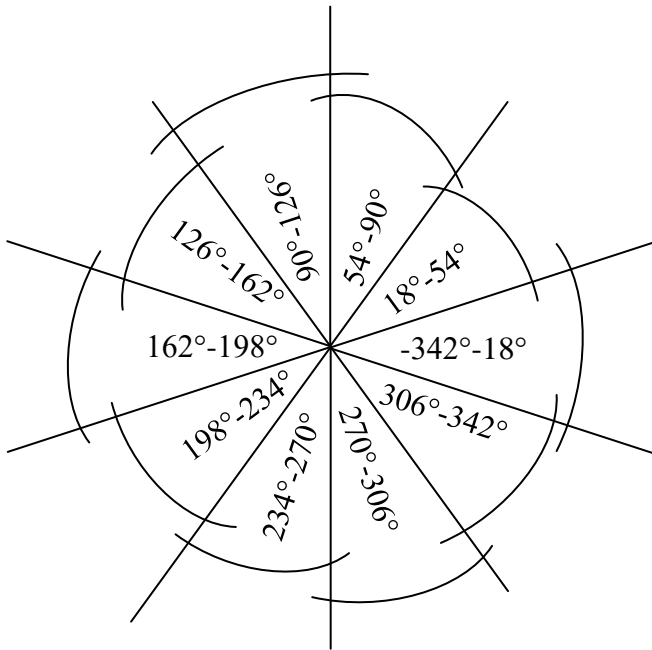


Fig. 1 Arrangement of antennas and their angle coverage in degrees used in 2.45 GHz band.

As mentioned in the introduction, directional antennas are used. Antennas are made on FR4 PCB. The principle of antennas is Yagi-Uda with 14 elements. The antennas are mounted on a 3D printed holder that holds the antenna firmly

at the right angle. The arrangement of the 2.4 GHz antennas is shown in Fig. 1. Every antenna covers approximately 36 degrees, so the total amount of antennas is 10, so they are able to cover 360°. The radiation pattern of the antenna at 2.45 GHz is shown in Fig. 2.

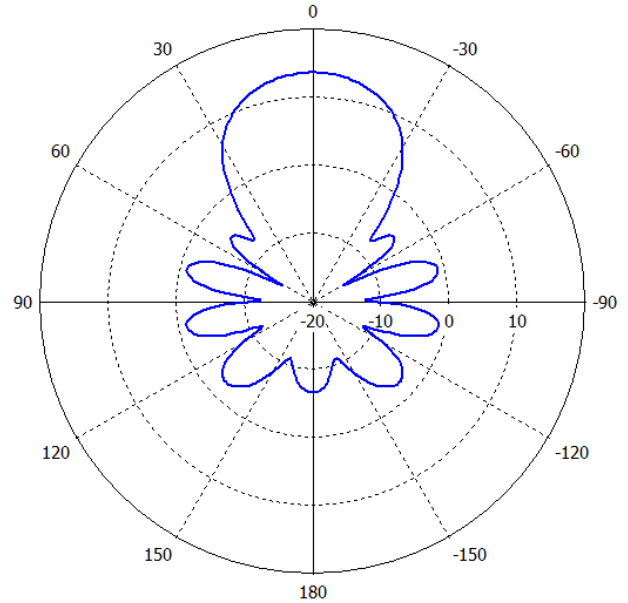


Fig. 2 Simulation of antenna H-plane radiation pattern at 2.45 GHz.

The 5 GHz antennas are not so directional, so there is not necessary to use many components as in 2.4 GHz configuration. The main lobe of the 5 GHz antenna covers an area wider than the 2.4 GHz antennas. The cover angle is almost 75°, so there are only 5 of these antennas used. The type of antenna is Log-periodic antenna made on PCB.

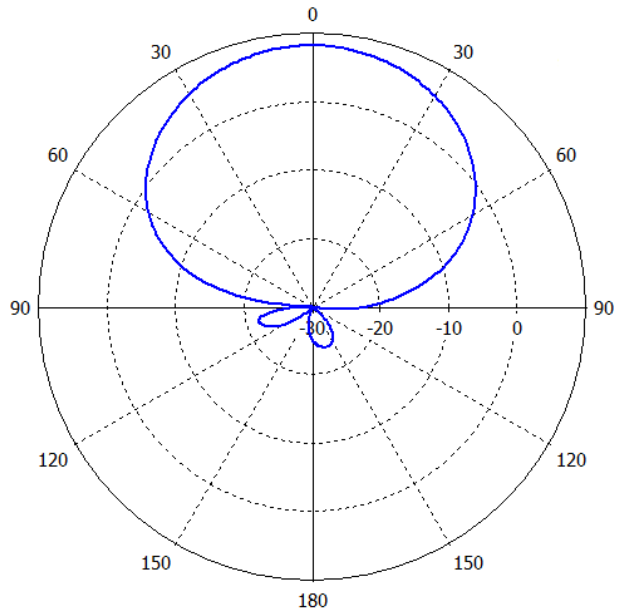


Fig. 3 Simulation of antenna H-plane radiation pattern at 5 GHz band.

### B. WiFi Module

The WiFi module used is SoC CYW43907, which is 802.11 a/b/g/n compliant. It can be used for both 20 and 40 MHz channels. The main advantage is promiscuity mode, which is a critical function where the module works as the watcher, so it only receives packets and is not visible in the network. The main advantage of this module is that it has two inputs for 2.45 and 5 GHz, so we can detect all access points.

The data which are sent by the module are SSID, RSSI, Channel number, and basic parameters of RF LNAs. The channels are continually scanned every 2.7 seconds – this is the total time of the full scan. For 2.45 GHz, 14 channels need to be scanned and for 5 GHz band even more. The position of the access point is calculated in the GUI. The value of RSSI of one AP is sent to the PC. The value of RSSI is different for all antennas due to the directivity of the antenna. From this value, the direction is calculated with the help of goniometric functions. From measurement was noticed that at all of the antennas the Access point could be measured due to back lobes of the antenna, but those values of RSSI are significantly lower. The AP is almost always higher in three antennas which set the direction, others are forgotten.

The disadvantage of this module was in its internal RF connection. The set gain of the low noise amplifier was not described in datasheet because it was only a preliminary version, and the RSSI value had a very high tolerance for our precise calculations. The tolerance was different for all configurations of channels. This must be included in these calculations.

#### Final Parameters

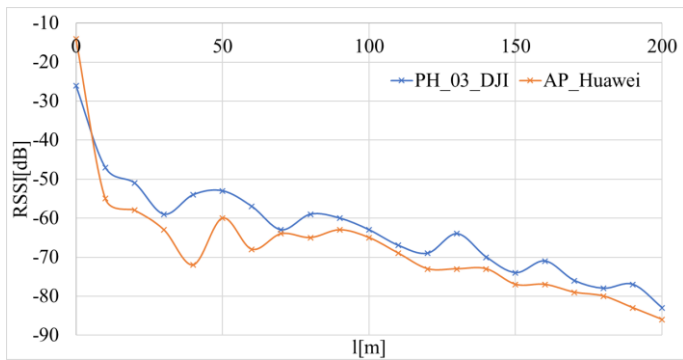


Fig. 4. Measured RSSI in dependence to distance for Access Point of Huawei mobile and the controller of DJI drone.

In Fig. 4 measured RSSI in dependence to the range is shown. Two APs were used as measuring devices. The first was a classic AP mobile phone and the second was a direct controller from DJI Phantom 3 drone. The maximum distance achieved was about 200 meters. As can be seen in the chart, there are four main jumps on the curve that are caused by the AGC of receiving LNA. Since the module was in the preliminary version, the feature of a manual set of the LNA could not be accomplished.



Fig. 5 Complete WiFi AP detector.

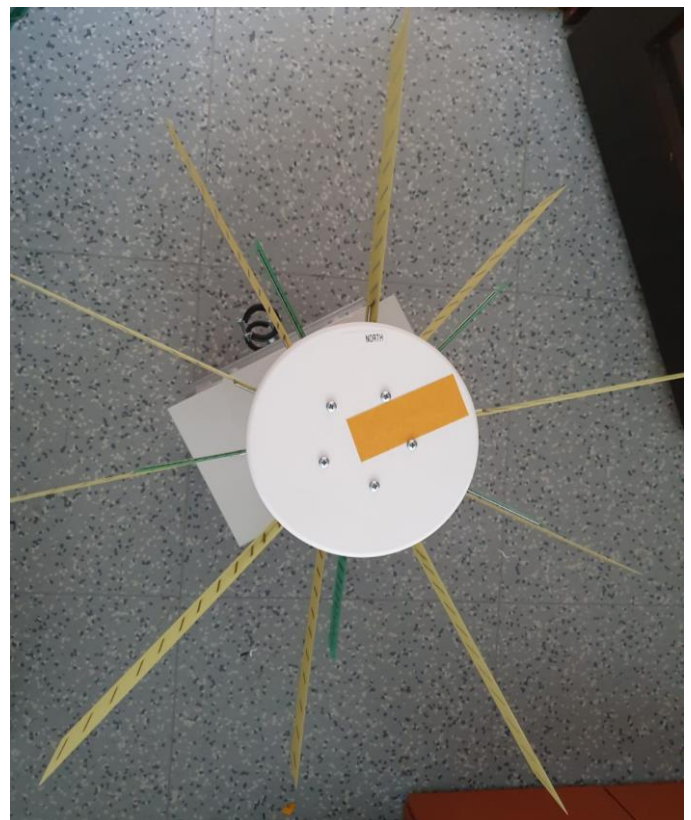


Fig. 6 View from the top.

The complete WiFi AP detector is shown in Fig. 5. The modules are covered in a white box on which the antenna holder is mounted. The box has its input for 12 V DC or 230 V AC. Also, the Ethernet port is on the box.

The arrangement of antennas is shown in Fig. 6. The angles between the antennas can be seen as well as the 5 GHz antennas for the 5 GHz band.

### III. CONCLUSION

This article was focused on WiFi detector, which was designed to locate the man who controls the drone. Drones have been in recent years, more and more accessible, and the threats are growing. This article gives the reader different perspective on this issue, where only locating the drone don't have to be the solution, because it can not always be jammed, but finding the man will solve this problem.

The detector has a simple idea when ten directional antennas were used, and with the scanning of all channels and obtaining the required parameters, the course of the man is received. From the goniometric function and the strength of the received signal, his course can be calculated.

The range of this detector version was about 200 meters, but the course was not as correct. The improvement could be done with custom boards where the coaxial cables do not need to be mounted, and the antenna will be on one PCB with the SoC that was the part of the development kit. The reduction board between antenna and module added more attenuation and more cross calls in the box where all modules were mounted.

This solution only works for drones with the ability to record video to a mobile phone, where it is the AP controller, and the video stream is transferred from the drone to the controller and from the controller to the mobile phone. If the drone controller has built display or does not even have a display, it cannot be tracked in this way.

As a prototype, this solution was successful, and it is expected that the results will be better in further research and with mentioned improvements.

### ACKNOWLEDGMENT (*Heading 5*)

The research described in this paper was financed by Czech Ministry of Education in frame of National Sustainability Program under grant LO1401. For research, infrastructure of the SIX Center was used. The research published in this submission was financially supported by the Brno University of Technology Internal Grant Agency under project no. FEKT-S-17-4713.

### REFERENCES

- [1] J. Park, D. H. Kim, Y. S. Shin and S. Lee, "A comparison of convolutional object detectors for real-time drone tracking using a PTZ camera," 2017 17th International Conference on Control, Automation and Systems (ICCAS), Jeju, 2017, pp. 696-699. doi: 10.23919/ICCAS.2017.8204318
- [2] D. Lee, W. Gyu La and H. Kim, "Drone Detection and Identification System using Artificial Intelligence," 2018 International Conference on Information and Communication Technology Convergence (ICTC), Jeju, 2018, pp. 1131-1133. doi: 10.1109/ICTC.2018.8539442
- [3] D. de Quevedo, F. I. Urzaiz, J. G. Menoyo and A. A. López, "Remotely Piloted Aircraft Detection with Persistent Radar," 2018 15th European Radar Conference (EuRAD), Madrid, 2018, pp. 317-320. doi: 10.23919/EuRAD.2018.8546546
- [4] S. Björklund, "Target Detection and Classification of Small Drones by Boosting on Radar Micro-Doppler," 2018 15th European Radar Conference (EuRAD), Madrid, 2018, pp. 182-185. doi: 10.23919/EuRAD.2018.8546569
- [5] G. Fang, J. Yi, X. Wan, Y. Liu and H. Ke, "Experimental Research of Multistatic Passive Radar With a Single Antenna for Drone Detection," in *IEEE Access*, vol. 6, pp. 33542-33551, 2018. doi: 10.1109/ACCESS.2018.2844556
- [6] K. Stasiak, M. Ciesielski, A. Kurowska and W. Przybysz, "A study on using different kinds of continuous-wave radars operating in C-band for drone detection," 2018 22nd International Microwave and Radar Conference (MIKON), Poznan, 2018, pp. 521-526. doi: 10.23919/MIKON.2018.8405275R. Nicole, "Title of paper with only first word capitalized," *J. Name Stand. Abbrev.*, in press.

# Optimization of Mel-Frequency Cepstral Coefficients for Automatic Gunshot Detection

Martin Hrabina

Department of Radio Electronics  
Brno University of Technology  
Brno, Czech Republic  
Email: hrabina@phd.feec.vutbr.cz

**Abstract**—Mel-frequency cepstral coefficients (MFCCs) are features widely used in tasks such as sound event detection (SED), speech recognition or other audio processing problems. This paper explores various ways of modification MFCCs in order to achieve optimal detection results for gunshot detection task. The paper focuses especially on frequency scale and bandwidth, number of filter banks and filter bank shape. The final results achieve recognition performance of 98.7 true negative rate (TNR) and 84.8 true positive rate (TPR).

**Keywords**—gunshot detection, mel-frequency cepstral coefficients, optimization

## I. INTRODUCTION

General audio event detection (AED) including gunshot detection is already well established field of research. The purpose varies from content retrieval [1], through surveillance [2] to wildlife protection [3] and other very specific requirements [4].

Key concepts in AED are based on extraction of features that describe the audio events of interest and pattern recognition algorithms. And features will be focus of this work. Some were tailored specifically for modeling speech (such as linear predictive coefficients - LPC or mel-frequency cepstral coefficients - MFCC) but later used for other sounds as well, some features use low-level concepts such as signal energy, or energy in spectral bands [5], zero-crossing rate [6] or correlation with templates. New convolutional neural networks use spectrograms for extraction of their own features that are based on 2D-pattern [8]. Some works use further feature reduction techniques such as linear discriminant analysis [4], principal component analysis [7] or maximum relevance minimum redundancy (MRMR) [8].

The MFCC parameters have become established as the basic feature vector for most acoustic pattern recognition problems. For this reason, any new and efficient way to optimize the recognition process is useful. This paper deals with an optimization of MFCCs by changing some parameters in order to improve performance of gunshot detection. The rest of the paper is structured as follows: chapter (II) describes audio dataset used throughout this paper, chapter (III) introduces MFCC extraction technique, chapter (IV) outlines our approach, introduces recognition algorithm and evaluation metrics and finally chapter (V) shows achieved results. Final chapter (VI) concludes the work, underscoring attained goals and outlines possible future work.

## II. AUDIO DATASET

Audio recordings used in this work come from two sources. First source, a set of 1532 gunshots from 25 different weapons comes from [9]. Each gunshot is in separate audio frame with length 486 samples. Second source is a collection of non-gunshot sounds in 6 classes (car horn, barking dog, drilling, idling engine, jackhammer and siren) proceeding from [10], each category consists of 4000 frames (of 486 samples), with each frame having normalized amplitude of at least 0.5. All sounds were recorded in lossless format (.wav or .flac), converted to mono (averaging multiple audio channels), downsampled to 44.1 kHz and quantized with 16-bits.

## III. MFCC EXTRACTION

Standard MFCC extraction consists of multiple steps, described in [11] and briefly outlined below. The first step is calculating decadic logarithm of power spectrum (1):

$$P(k) = \log_{10}(|FT(s(n))|^2), \quad (1)$$

where  $k$  is index of power spectrum and  $|FT(s(n))|^2$  is a square of magnitude of Fourier transform of discrete input signal  $s(n)$ , i.e. the power spectrum. Afterwards, the signal is filtered using  $N$  filter banks, usually of triangular shape, thus obtaining  $N$  frequency bank energies (2):

$$X_n = P(k)\phi_n(k), \quad (2)$$

where  $X_n$  is energy in  $n$ -th filter bank,  $P(k)$  is power spectrum at index  $k$  and  $\phi_n$  is transfer function of  $n$ -th filter bank. Filter bank boundaries are usually calculated on nonlinear mel-scale, which can be obtained from frequency scale in Hz using mel warping function (3):

$$f_{mel} = 1127 \cdot \ln\left(1 + \frac{f}{700}\right), \quad (3)$$

where  $f_{mel}$  is frequency in mels and  $f$  frequency in Hz. Upper boundary of  $n$ -th filter is then defined as (4):

$$k_{bn} = f_{mel_{lo}} + n + \frac{f_{mel_{hi}} - f_{mel_{lo}}}{N + 1}, \quad (4)$$

where  $f_{mel_{lo}}$  and  $f_{mel_{hi}}$  is lowest and highest frequency respectively in mels,  $N$  is the number of filters and  $n$  is index

of particular filter. These filter banks are introduced to simulate filtering inside auditory critical bands and masking phenomena in humans.

The final step is to apply discrete cosine transform (5) to filter bank energies, obtaining  $M$  MFCC coefficients.

$$c_m = \sum_{n=1}^N (X_n \cdot (\frac{\pi}{N} m(n - 0.5))), \text{ for } m = 1, 2, \dots, M. \quad (5)$$

In this equation,  $c_m$  is  $m$ -th MFCC coefficient and  $X_n$  is  $n$ -th filter bank energy. Sometimes, cepstral liftering is applied as a post-processing step.

#### IV. METHOD

As mentioned in chapter I, MFCC are frequently used in various audio recognition tasks, however usually not much attention is paid to (or at least mentioned) the various possibilities MFCC extraction process offers. This paper tweaks different points in MFCC calculation to discover the best combination for the task of gunshot detection. The baseline setup starts with 40 triangular filter banks on a mel scale with bandwidth 8 kHz, using 20 coefficients.

MFCC are defined on a mel scale with (3), the first step is going to be to remove this nonlinear distribution of filter boundaries and use linear distribution instead (thus, using Hertz scale, not mel-scale). Another parameter, having to do with the very first step (3), is to vary input bandwidth, with values beginning at 4 kHz and going up to 16 kHz. Now, all these experiments were using the same amount of filter banks and coefficients, so this paper also tries to vary the number of filter banks (with increasing bandwidth) and keeping filter bank to coefficient ratio of 0.5 (i.e. having half as much coefficients in comparison to number of filter banks), variation of filter bank to coefficient ratio is interesting area as well, thus the end of the chapter will provide only a glimpse of how changing the number of coefficients affects recognition performance. The last thing that will be modified, is filter shape. The basic definition presupposes triangular filter banks, but other authors publication were experimenting also with different shapes [12]. This paper uses gammatone, rectangular and two kinds of exponential filters, apart from traditional triangular filter shape.

These feature setups were evaluated based on their performance in binary gunshot recognition task. In order to estimate their performance, neural networks were used as recognition algorithm. Neural networks were chosen because of their use in state-of-the-art approaches and implemented using Matlab. The architecture consists of two hidden layers with 20 neurons each, because this setup provided the best results in previous tests. The input is normalized to mean value 0 and standard deviation of 1 using training data, layers use sigmoid activation function and each layer is followed by batch normalization, last layer uses softmax function to decide between gunshot and non-gunshot output. For training and testing, data described in chapter II was used, along with 5 rounds of training/testing per feature to ensure different starting conditions and suppress effect of training/testing subset choice. Each round consisted of randomly drawing 1000 frames from each class (obtaining 7000 frames total) using predetermined seed for ensuring

repeatability, this was divided into training subset (70%), validation subset (15%) and testing subset (15%). Results from each round were averaged, and this average constituted result for given feature setup.

Evaluation metrics consist of true positive rate (TPR), defined by (6) and true negative rate (TNR), defined by (7):

$$TPR = \frac{TP}{P} = \frac{TP}{TP + FN}, \quad (6)$$

$$TNR = \frac{TN}{N} = \frac{TN}{TN + FP}, \quad (7)$$

where  $P$  is total number of positives (i.e. gunshots),  $TP$  is number of true positives (gunshots identified as gunshots) and  $FN$  is number of false negatives (missed gunshots detections). Analogously,  $N$  is number of all negatives (that is, all non-gunshot frames),  $TN$  number of true negatives (non-gunshot frames identified as such) and  $FP$  number of false positives (a.k.a. false alarms - number of non-gunshot frames identified as gunshots).

#### V. EVALUATION AND RESULTS

To find out the best feature setup, one setup was chosen as default, and parameters were progressively changed until arriving at best performing set. This methodology does not explore all possible combinations (comprehensive grid search), thus there is a possibility that other combination would perform even better, but it nevertheless discovers setup performing better than initial setup. When time is not a constraint, grid search is recommended to discover the very best combination. Also, not all parameters were varied, some of unexplored possibilities will be mentioned in conclusion.

The basic setup is using mel scale with bandwidth of 8 kHz, 40 filter banks using triangular filters and 20 coefficients. The first step is to try to change nonlinear scale for linear. Tab. I below shows that linear scale provides far better results in terms of TPR.

After establishing that linear scale is more advantageous, effects of bandwidth with invariant and changing number of filter banks (while retaining coefficient to filter bank ratio roughly stable, at 0.5). Tab. II and Tab. III show the results of the two above mentioned changes respectively. Increasing bandwidth (with starting frequency at 0 Hz) itself yielded mixed results (initial decrease, then increase), however when the number of filter banks is increased as well, dramatic increase in recognition performance is noted.

TABLE I. MFCC WITH MEL AND LINEAR FREQUENCY SCALES

Scale	TNR [%]	TPR [%]
linear	97.4	73.0
mel	97.4	57.9

The final modification undertaken is changing the filter bank shape (transfer function of the filter). Tab. IV presents various filter bank shapes along with their attained scores, while retaining the best options so far, i.e. bandwidth of 16 kHz with 41 filter banks on linear scale and 20 coefficients. The

TABLE II. MFCC WITH INCREASING BANDWIDTH

Bandwidth [kHz]	TNR [%]	TPR [%]
4	97.3	75.3
8	97.4	73.0
12	98.0	69.1
16	98.3	77.5

TABLE III. MFCC WITH INCREASING BANDWIDTH AND NUMBER OF FILTER BANKS

# coefficients	# filter banks	Bandwidth [kHz]	TNR [%]	TPR [%]
12	24	4	86.3	61.5
16	32	8	97.3	71.0
18	37	12	97.7	73.0
20	41	16	98.5	83.0

scores vary considerably, with exponential function achieving the worst results, and gammatone the best, right after triangular (in both TNR and TPR).

TABLE IV. MFCC WITH CHANGING FILTER BANK SHAPE

Filter bank shape	TNR [%]	TPR [%]
triangular	98.5	83.0
exponential	98.1	66.8
gammatone	98.7	84.8
rectangular	98.3	80.2

The best performing configuration so far is MFCC with 41 gammatone filters on a linear bandwidth of 16 kHz, using 20 coefficients. Since the only parameter we did not vary was the number of coefficients, Fig. 1 below presents dependency of TNR and TPR on the number of coefficients in the above mentioned configuration. Thus the final configuration achieves even better results while using 18 coefficients instead of 20, with TPR equal to 87.2% and TNR equal to 98.6%.

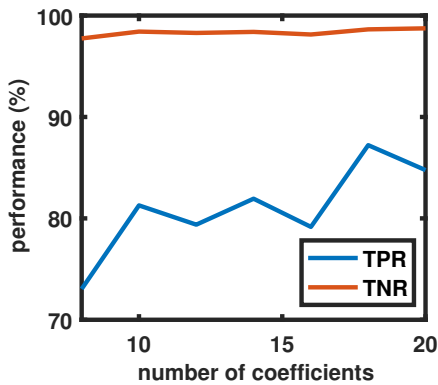


Fig. 1. MFCC with changing number of coefficients

## VI. CONCLUSION

The aim of this paper was to pay attention to frequently ignored parameters during MFCC extraction process and tweaking them in order to obtain better recognition results. Apart from modifying the most obvious parameters, such as number of coefficients, we are also looking at slightly less modified ones (e.g. frequency, number of filter banks), but also on those very rarely looked at (frequency scale and filter bank

shape). The results show an increase of almost 30% in TPR, which is to a degree caused by suitability of dataset. But more importantly, the results indubitably hint that MFCC extraction parameters are full of possibilities to improve performance that are often overlooked. In order to discover the optimal setup, extensive grid search is recommended, time and resources allowing. Apart from this obvious aim of the paper, another interesting point would be to use different MFCC setups in an ensemble of recognition algorithms, with each setup serving one algorithm (such as different neural network). This extended use might further improve recognition performance and is definitely worth exploring.

## REFERENCES

- [1] T. Giannakopoulos, A. Makris, D. Kosmopoulos, S. J. Perantonis, and S. Theodoridis, "Audio-visual fusion for detecting violent scenes in videos," in *6th Hellenic Conference on Artificial Intelligence: Theories, Models and Applications*, vol. 6040, 05 2010, pp. 91–100.
- [2] L. Gerosa, G. Valenzise, M. Tagliasacchi, F. Antonacci, and A. Sarti, "Scream and gunshot detection in noisy environments," in *2007 15th European Signal Processing Conference*, Sep. 2007, pp. 1216–1220.
- [3] M. Hrabina and M. Sigmund, "Acoustical detection of gunshots," in *2015 25th International Conference Radioelektronika (RADIOELEKTRONIKA)*, April 2015, pp. 150–153.
- [4] Y. Wang, B. Sun, X. Yang, and Q. Meng, "Heart sound identification based on mfcc and short-term energy," in *2017 Chinese Automation Congress (CAC)*, Oct 2017, pp. 7411–7415.
- [5] C. Clavel, T. Ehrette, and G. Richard, "Events detection for an audio-based surveillance system," in *2005 IEEE International Conference on Multimedia and Expo*, July 2005, pp. 1306–1309.
- [6] E. akr, G. Parascandolo, T. Heittola, H. Huttunen, and T. Virtanen, "Convolutional recurrent neural networks for polyphonic sound event detection," *IEEE/ACM Transactions on Audio, Speech, and Language Processing*, vol. 25, no. 6, pp. 1291–1303, June 2017.
- [7] J. Portelo, M. Bugalho, I. Trancoso, J. Neto, A. Abad, and A. Serralheiro, "Non-speech audio event detection," in *2009 IEEE International Conference on Acoustics, Speech and Signal Processing*, April 2009, pp. 1973–1976.
- [8] E. Kiktova, M. Lojka, M. Pleva, J. Juhar, and A. Cizmar, "Gun type recognition from gunshot audio recordings," in *3rd International Workshop on Biometrics and Forensics (IWBF 2015)*, March 2015, pp. 1–6.
- [9] S. N. Media. The free firearm sound effects library. [Online]. Available: <https://www.stillnorthmedia.com/firearm-sound-library.html>
- [10] J. Salamon, C. Jacoby, and J. Bello, "A dataset and taxonomy for urban sound research," in *Proceedings - 22nd ACM International Conference on Multimedia*, 11 2014.
- [11] A. C. Kelly and C. Gobl, "A comparison of mel-frequency cepstral coefficient (mfcc) calculation techniques," in *Journal of Computing*, 2011.
- [12] I. Jokic, V. Delic, S. Jokic, and P. Zoran, "Automatic speaker recognition dependency on both the shape of auditory critical bands and speaker discriminative mfccs," *Advances in Electrical and Computer Engineering*, vol. 15, pp. 25–32, 11 2015.

# Advanced Methods of Lightning Protection in Composite Aircraft

David Krutilek  
Engineering Services Division  
Evektor, spol. s r.o.  
Kunovice, Czech Republic  
dkrutilek@evektor.cz

**Abstract**— This paper reports the current state-of-the-art systems on lightning strikes, their effects on composite aircraft, and new techniques available to engineers and operators to safeguard against detrimental effects of lightning strikes. Manufacturing and designing of composite aircraft need some advanced strategies and engineering applications to sustain the same degree of safety and shelter as achieved by conductive aluminum skinned aircraft.

**Keywords**—lightning strike protection; thermal spray coating; tufting of composite structures; composite; CFRP

## I. INTRODUCTION

Carbon fibre reinforced polymer (CFRP) features in the latest generation of aircraft such as the Boeing 787, Airbus A350 and Bombardier C-Series, as well as smaller aircraft such as the Evektor EV-55. One of the biggest problems in building and certifying an all-composite airframe is lightning protection. Traditionally, lightning strike protection on composite aircraft components has been provided by embedding expanded metal foil just below the surface of fibre reinforced composites during manufacture. However, this is a costly, highly specialised manual process.

One of the biggest problems in building and certifying an all/semi composite airframe is lightning protection. On average a plane is struck once every 1000-3000 flight hours, equivalent to one strike per aircraft per year. An aircraft modifies the electric fields in its vicinity, which acts as a catalyst for lightning attachments, hence the high strike rates whilst the plane is airborne. Despite this a worst-case strike is only likely to occur every 10-15 years. Unprotected composite material can be completely blown apart by a lightning strike (up to 200,000A). This occurs because carbon fibre epoxy is 1000 times more resistant to current flow than aluminum. This high resistance converts the current flow of the strike into heat energy.

Different parts of the aircraft are zoned (Figure 1) according to the risks of a lightning strike as shown below [1]. Area such as the nose and wing tips are at greatest risk of lightning strike attachment (entry or exit). Other areas may be less likely to be subject to an attachment but may still carry substantial currents and thus different areas of the aircraft are

zoned according to the type and likelihood of lightning strike attachment (Fig 1).

- Zone 1A (first return stroke zone) where the first return stroke has very a little probability of flash hang-on.
- Zone 1B (first return stroke with long hang-on) initial attachment point with greater probability of lightning channel hang-on.
- Zone 1C (transition zone for first return stroke) where the first return stroke with reduced-amplitude has a probability of lightning channel hang-on.

The structural parts that are considered in Zone 1 are also considered in Zone 2, since they experience restrike and current sweeps around them. These structural parts include the majority of the structure of the aircraft. In the past, the fuselage and engine nacelle were made of aluminum skin that can easily sustain Zone 1A lightning current. Replacement of aluminum skin with composite, however, make this aspect of lightning much more complicated.

- Zone 2A (swept stroke zone) is a zone with low probability of lightning channel hang-on.
- Zone 2B (swept-stroke zone) a swept-stroke zone with high probability of lightning channel hang-on.
- Zone 3: The portion of the airframe in an aircraft that lie within or between the zones, and carry significant amount of current due to conduction in the aircraft structure.

Zones are the channels through which the external environment is applied to the structure of an aircraft. Generally, the locations of these zones depend on the geometry of an aircraft, operating features and materials and often vary from one aircraft to another. In modern airplanes, the most of the exterior airframes that belong to these zones are manufactured from either carbon fiber reinforced polymers or glass fiber-reinforced polymers, which are not good electrical conductors. In order to address the issue of low electrical conductivity of these materials various solutions of lightning strike protection (LSP) have been available. These solutions can be divided into two categories applying diverter strips or bar on the exterior

surface of the aircraft, and the use of electrically conductive materials on the exterior surface of composite aircraft structures.

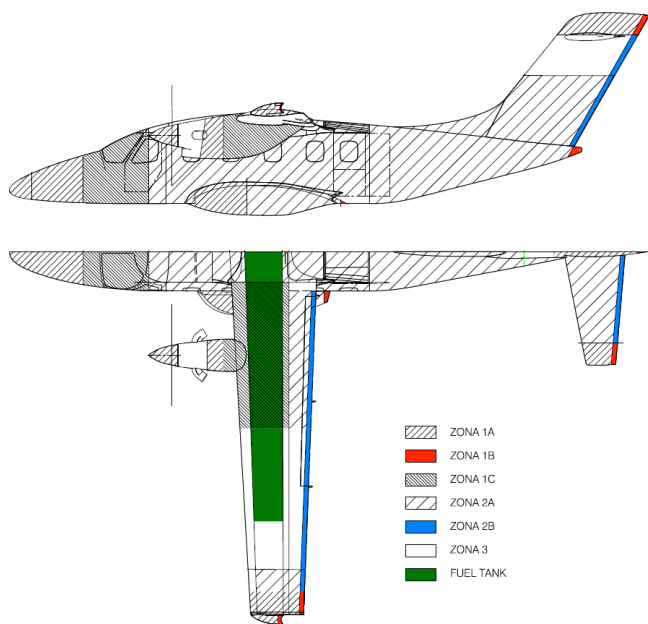


Fig. 1 Lightning strike zoning diagram of the EV-55 aircraft

Traditionally, lightning strike protection on composite aircraft components has been provided by embedding expanded metal foil just below the surface of fibre reinforced composites during manufacture. Whilst continuous expanded metal foil outperforms all other present ductile material options, it is very difficult to apply over concave and convex surfaces, and particularly compound angles. It is a costly, highly specialised manual process.

## II. COLD SPRAYING PROCESSES

The fundamental principles of all thermal spraying processes are similar, ie powder or wire consumables are heated by oxy fuel combustion (flame and HVOF) or electrically (arc and plasma) until molten or soft, and propelled at speed onto a substrate to form a coating. A wide range of materials can be applied by thermal spraying as long as the consumable (metal, ceramic, cermet or polymer) is available in powder or wire form suitable for the spray process. The density of the coating is dependent on the material composition, its state on impact (solid/liquid ratio) and the particle impact velocity. The bond between a sprayed coating and the substrate is primarily mechanical, with some metallurgical bonding. Adhesion of the coating to the substrate depends not only on spray particle condition but also the condition of the substrate surface, which must be clean and roughened by grit blasting or machining prior to spraying. Thermal spraying is divided into five main categories, including the relatively new cold spraying process [5-8]:

- Flame spraying
- Arc spraying
- Plasma spraying
- High velocity oxyfuel (HVOF) spraying
- Cold spraying

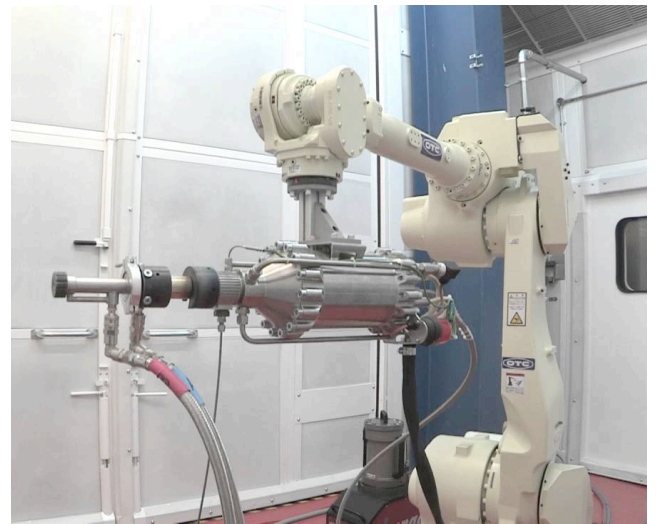


Fig. 2 Cold Spray System from TWI

Attempts have been made to deposit a wide variety of coating materials directly on composites using wire flame spraying, twin wire arc spraying, HVOF, plasma spraying and cold spraying. However, considerable care must be taken to control the temperature of the substrate during the spraying process and to avoid degradation due to erosion. Cold spraying was considered as an ideal technique for the deposition of electrical conductive coatings as the powder particles are deposited in the solid state at relatively low temperature, and thus oxidation is minimized. However, the high velocity of the particles erodes the substrate, exposing and fracturing the carbon fibers.

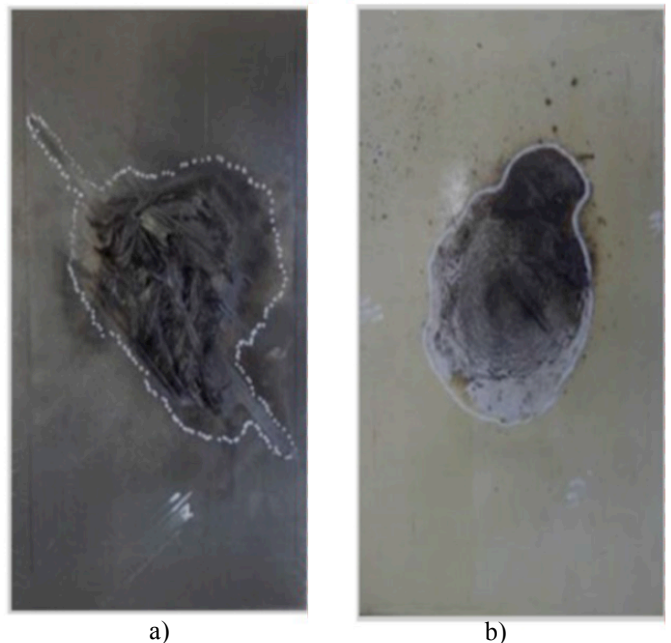


Fig. 3 Composite panels after zone 2A lightning strike: (a) composite-reinforced panel without protection (b) composite-reinforced panel with a full-sprayed aluminum coating [9]

For the two different types of aircraft carbon fiber/epoxy composite-reinforced panels, the surface damage pattern and size due to lightning strikes is shown in Fig. 3. The composite panel without protection was the most serious, caused by fiber

fracture and matrix cracking, resin vaporization, delamination, etc. Lightning damage propagated significantly along the fiber direction. For lightning protection structures, lightning strikes can result in the melting of metal covers, and composite damage is inevitable. The melting of the metal coating was propagated outward from the attachment point of the lightning arc. It can be seen that the surface damage area of the lightning protection structures was larger than that of structures without protection, and the local-sprayed aluminum coating had the largest damage area. Although the metal covers were damaged, the composite-reinforced panels underneath were protected from lightning strikes, and composite damage was decreased to some extent.

### III. TUFTING OF COMPOSITE MATERIALS

This chapter reports the development of multifunctional composites based on the use of metallic tufting. Stainless steel and copper are used to modify the through thickness mechanical and electrical behaviour of epoxy/carbon composites. The mechanical performance is evaluated in mode I delamination and the electrical behaviour is assessed using conductivity measurements and lightning strike tests. Metal tufting improves the delamination resistance by approximately 200% and 100% and the through thickness conductivity by 250 and 20 times for copper and stainless steel reinforcement, respectively. Lightning strike damage is suppressed significantly, with internal damage decreasing by about 90% and 75% compared to unprotected laminates for copper and stainless steel tufting, respectively. In the case of copper tufting the protection is comparable to what is achieved by standard surface copper mesh. These findings show that copper tufted composites are an ideal solution in applications requiring advanced mechanical and electrical functionality.

The utilisation of composites in aerospace structures, which is mainly driven by their mechanical characteristics and associated weight benefits, is associated with challenges related to the electrical behaviour of these materials. The low electrical conductivity of carbon composites in the through thickness direction compared to their metallic counterparts makes their response to lightning strike problematic. The solution adopted in the industry is to integrate metallic elements in composite structures in the form of meshes, foils or interwoven fabrics attached to the surface of the component. These protective elements dissipate the current through the surface of the component and minimise or eliminate direct and indirect lightning strike damage. The integration of metallic elements comes at a cost linked to the addition of an extra manufacturing step for the integration of the mesh. Furthermore, potential repair of the structural component due to lightning strike or other types of damage becomes more challenging and costly as the removed protection layer needs to be replaced and the added material connected electrically to the rest of the protective layer.

Metallic tufts are capable of reinforcing composite structures significantly increasing the delamination toughness in mode I. The tensile behaviour of the tuft has significant impact on the delamination toughness. In the case of the ductile copper wire the high ultimate strain allows several tuft rows to bridge the crack simultaneously leading to very high

delamination toughness and progressive failure. The incorporation of metallic tufts increases significantly the through the thickness conductivity of composites. This is reflected in significantly better lightning strike performance, which in the case of copper tufting matches the performance of standard protection methods such as the use of copper mesh. Furthermore, the use of tufting changes significantly the electrical behaviour during lightning strike as current can be dissipated through the thickness in contrast to surface dissipation which is dominant in standard protection methods. This leads to a reduction in surface damage.

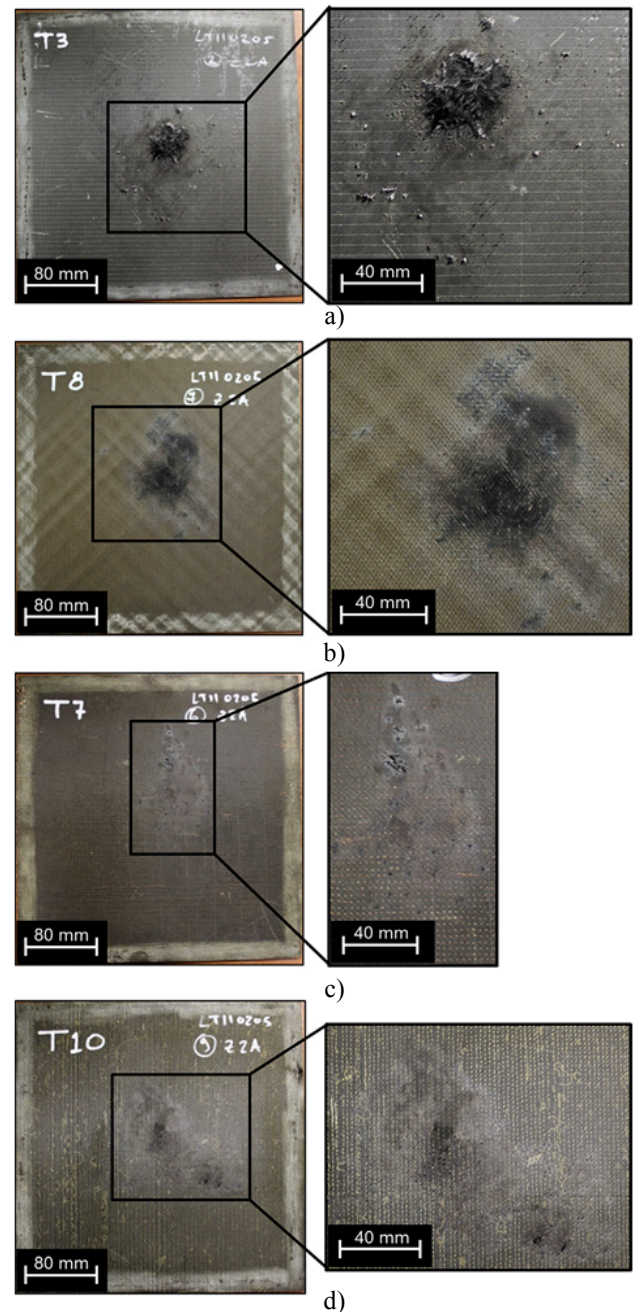


Fig. 4 Composite panels after zone 2A lightning strike: (a) untufted control, (b) untufted control with copper mesh, (c) copper tufted and (d) stainless steel tufted. [10]

Fig. 4a and 4b shows the untufted composite panels after Zone 2A lightning strike. The untufted unprotected panel displays the greatest damage in the form of extensive resin burn off and an extended area of fibre fracture and splintering in the centre, as shown in Fig. 4a. The latter type of damage can be considered as critical and could deteriorate the structural integrity of the structure in operation. The small damage regions outside the central area are caused by return strokes of lower current amplitude. Protecting the untufted control panel with a copper mesh reduces the damage significantly, as shown in Fig. 4b. The highly conductive mesh conducts the current along the surface of the composite, reducing the energy density at the attachment location, preventing major fibre fracture and leading to a central area of surface resin burn off and a small amount of out of centre damage caused by return strokes. A small area of fibre fracture present in the centre is caused by the lightning strike in an area that is associated with damage and vaporisation of the copper mesh. This result demonstrates the benefits of the standard solution of incorporating a conductive surface layer in the composite as the type of damage is mostly non critical resin burn off rather than extensive fibre fracture. The case of the copper tufted composite panel is shown in Fig. 4c. It can be observed that the high conductivity of the copper tufts leads to a very small amount of damage in the centre of the panel accompanied by a few spots of resin burn off away from the centre as a result of return strokes. The current is dissipated successfully through the copper wire tufts leading to significant damage reduction in comparison to the unprotected laminate.

The results with stainless steel tufts follow a similar trend (Fig. 4d). The panel shows several spots of resin burn off due to return strokes and a small spot of fibre tufting due to the first lightning attachment. The relatively small overall damage, compared to the unprotected control panel is due to the higher through thickness conductivity of the stainless steel laminate. The overall damage in the stainless steel tufted panel appears greater than in the copper tufted material and the mesh protected laminate, which can be attributed to the lower electrical conductivity of steel compared to copper.

#### IV. CONCLUSIONS

In this article, two new technologies were introduced to protect the composite parts of the aircraft from lightning strikes, namely cold spraying and tufting. The advantage of these technologies is undoubtedly higher effectiveness of lightning protection, which was confirmed by tests. Other advantages include relatively easy application and adaptation to LSP requirements, as well as non-aerodynamic disturbance and possible easy reparability. The deployment of these technologies in the aerospace industry in mass production of aircraft will also reduce the cost of application. As a secondary effect of using these technologies, shielding against high intensity radiated field (HIRF) is better.

#### ACKNOWLEDGMENT

This work has been funded by Evektor, spol. s r.o. and the Clean Sky2 – AIRFRAME – WP-B-3.4.2. project consortium.

#### REFERENCES

- [1] Morgan D, Hardwick C J, Haigh S J and Meakins A J (Cobham): 'The Interaction of Lightning with Aircraft and the Challenges of Lightning Testing', Journal of Aerospace Lab, Issue 5 - December 2012, pl-10
- [2] Shackette L W, Kulkarni V G, Wessling B, 1991; 'EMI shielding of intrinsically conductive polymers', Society of Plastic Engineers, Technical Conference, 37, pp665-667
- [3] Weinhold P D, Mehoke D S, 1998; 'EMI shielding effectiveness, surface resistivity and RF conductivity of thin composites for spacecraft applications', 30th International SAMPE Technical Conference, pp243-255
- [4] Harris G, Lennhoff J, Nassif J, Vinciguerra M, Rose P, 1999; 'Lightweight highly conductive composites for EMI shielding', Advanced Materials and Processes, 31st International SAMPE Technical Conference, 31, Pp 122-129
- [5] Pawlowski L, 1996; 'The Science and Engineering of Thermal Spray Coatings, First Edition', John Wiley and Sons Ltd. ISBN 0-471-95253-2.
- [6] Pawlowski L, 2008; 'The Science and Engineering of Thermal Spray Coatings, Second Edition', John Wiley and Sons Ltd. ISBN 978-0-471-49049-4.
- [7] Tucker RC (Ed); 'ASM Handbook Vol SA Thermal Spray Technology' ASM International, 2013. ISBN 978-1-61503-996-8.
- [8] Fauchais PL, Heberlein JYR, Boulos MI; 'Thermal spray fundamentals — from powder to part' Springer, 210, ISBN 978-0-387-28319-7.
- [9] Wang, F.; Ma, X.; Zhang, Y.; Jia, S. Lightning Damage Testing of Aircraft Composite-Reinforced Panels and Its Metal Protection Structures. Appl. Sci. 2018, 8, 1791
- [10] D.M. Lombetti and A.A. Skordos. Lightning strike and delamination performance of metal tufted carbon composites. Composite Structures, Volume 209, 1 February 2019, Pages 694-699